Accurate numerical prediction of ductile fracture and micromechanical damage evolution for Ti6Al4V alloy

Carlos Rojas-Ulloa[a], Víctor Tuninetti[b,*], Héctor Sepúlveda[c], Ehssen Betaieb[a], Gonzalo Pincheira[d], Gaëtan Gilles[e], Laurent Duchêne[a], Anne Marie Habraken[a,f,*]

[a] ArGEnCo Department, MSM team, University of Liège, Quartier POLYTECH 1, 9 allée de la Découverte, 4000 Liège, Belgium

[b] Department of Mechanical Engineering, Universidad de La Frontera, Francisco Salazar 01145, Temuco 4780000, Chile

[c] Magíster en Ciencias de la Ingeniería, Facultad de Ingeniería y Ciencias, Universidad de La Frontera

[d] Department of Industrial Technologies, Faculty of Engineering, Universidad of Talca, Camino a Los Niches Km 1, Curicó 3344158, Chile

[e] Centre d'exploitation et de compétence Samtech, Siemens Industry Software NV, Liège Science Park, 8 Rue des Chasseurs-Ardennais, 4031 Angleur (Belgium)

[f] Fonds de la Recherche Scientifique −F.R.S.−F.N.R.S. Belgium, 5 rue d'Egmont 1000 Bruxelles, Belgium

* Corresponding authors: victor.tuninetti@ufrontera.cl (V.T.); anne.habraken@uliege.be (A.M.H.); Tel.: +56452325984 (V.T.); +32496607945 (A.M.H.)

Highlights:

- Finite element implementation of a damage law
- Prediction of coalescence onset via a Thomason-based criterion
- Validated anisotropic elastoplastic and damage behaviour model for Ti6Al4V
- Prediction of the fracture propagation by damage mapping

This is a preprint article. The version of Record is published in Computational Mechanics, and is available online at https://doi.org/10.1007/s00466-023-02362-3

Citing version of Record:
Rojas-Ulloa, C., Tuninetti, V., Sepúlveda, H. et al. Accurate numerical prediction of ductile fracture and micromechanical damage evolution for Ti6Al4V alloy. Comput Mech (2023). https://doi.org/10.1007/s00466-023-02362-3

Abstract

A CPB06-based Stewart-Cazacu micromechanical damage model is implemented and validated for Ti6Al4V material. It provides accurate numerical predictions in terms of macromechanical material response and damage accumulation. The SC11−TNT damage model is implemented in the finite element (FE) software Lagamine following a semi-implicit cutting plane algorithm and a well-chosen flow rule approach. The damage of the material is characterized by the porosity ratio contained within the material. It is modelled by void nucleation, growth and coalescence mechanisms. The onset of the coalescence is established by a criterion based on Thomason's approach. The macroscopic results obtained by the implemented model demonstrate a strong ability to predict the experimental elastoplastic mechanical behaviour of the material across a full deformation range and different types of loadings. At the microscopic level, the predicted accumulated porosity ratio of the material matrix at fracture exhibits a good correlation with the experimental observations. The element deletion feature, activated when a certain damage threshold is reached, provides a physical description of the loss of load-carrying capacity of the material during fracture.

Keywords: CPB06 yield criterion; Coupled damage law; Ductile fracture; Thomason coalescence criterion; Ti6Al4V titanium alloy

---

Statements and Declarations

The authors declare that they have no known financial or non-financial interests that are directly or indirectly related to the work submitted for publication.

1. Introduction

The development of a validated model for the damage accumulation and the fracture prediction of samples in Ti6Al4V alloy is the focus of this article. The interests of such a research on this anisotropic damage model are presented hereafter.

Titanium alloys are known to exhibit excellent mechanical properties, such as high strength-weight ratio, exceptional corrosion resistance, good weldability, good biocompatibility, and the capability of withstanding high temperatures. They are thus considered ideal for manufacturing critical components in aerospace, chemical, shipbuilding, biomedical and defence industries. The relatively high-cost of Ti alloys is related to the particularly complex metallurgic processes involved in their production [1]. First developed in the 1950s, the Ti6Al4V titanium alloy (also known as "TA6V" or "Ti64") is to date the predominant Ti alloy in the worldwide market. Its microstructure is formed by a main α-Ti phase of hexagonal closed packed (hcp) crystals embedded in a β-Ti matrix phase of body-centred cubic (bcc) crystals [2]. Combined with the anisotropic and asymmetric behaviour of the α phase materials, the macromechanical response of the biphasic Ti6Al4V alloy is particularly complex [3], exhibiting orthotropic properties, a strength differential (SD) effect and a distortional hardening (DH) [4–7].

The material high-cost and the challenging numerical modelling of Ti6Al4V behaviour are the underlying factors explaining the high amount of current industrial and research interests to develop new synthetization techniques, manufacturing processes, and accurate numerical predictions of the deformation response of this alloy.

Non-coupled ductile damage criteria are still studied nowadays due to their relative simplicity and computational efficiency [8–10]. For these criteria, the fracture occurs when a damage indicator threshold is reached. The criterion can be a function of the stress triaxiality [11, 12], a Lode angle and stress triaxiality relationship [13, 14], a stress-strain relationship [15, 16], or a function based on a damage micromechanics variable [9]. Apart from some more complex

formulations [17], the inability of many of these models to find a unified set of parameters capable of accurately predicting fracture under any type of material loadings is continuously highlighted as their main drawback. In particular, the coupled prediction of the elastoplastic behaviour and the fracture of Ti6Al4V undergoing complex and large plastic deformations require that both damage accumulation and its effect on the local load carrying capacity of the material are taken into account (see conclusion of Tuninetti et al. [18]).

The experimental confirmation of the ductile fracture mechanisms was only possible after new imaging techniques enabled the in situ observation of the evolution of dimples embedded in the microstructure of largely deformed specimens [19, 20]. This knowledge entailed the development of new analytical formulations in fracture mechanics, considering a ductile fracture not as a stress or strain threshold but as a continuum micromechanics process of nucleation, growth and coalescence of micro voids driven by plastic deformations [11, 21–26]. Further studies on the interaction between porosity evolution and mechanical response led to the development of the well-known Gurson damage law [27]. The void growth model considered within the original Gurson formulation was later expanded towards nucleation and coalescence in the form of the Gurson-Tvergaard-Needleman (GTN) model [28, 29]. Overall, these pioneering formulations formed the basis for further studies and development of more reliable and physically accurate plasticity-damage models and ductile fracture criteria. The developments and the applications of coupled Gurson-type damage laws are now addressing yield criteria such as von Mises [30], Hill 48 [31], Hosford [32], CPB06 [33, 34] and CPB06ex2 [35]. More specialized developments oriented towards modelling of coupled damage prediction under cyclic fatigue loadings using Chaboche-type constitutive models can also be found [36].

Founded on the principles of analytical continuum mechanics with consideration of crystal anisotropy and tension-compression asymmetry exhibited by hcp alloys, Cazacu et al. [37] developed the CPB06 yield criterion. Implemented into Lagamine FE research software [38], in conjunction with a broad material experimental campaign (tensile and compression tests on

smooth samples in different directions, shear tests, tensile tests on notched bars, nano-indentation on different planes), this yield criterion demonstrated high accuracy in the prediction of the elastoplastic behaviour of Ti6Al4V alloy at both macro-mechanical [4–6, 18, 39] and nano-mechanical [2, 40] length scales. Note that Lagamine FE code is developed since 1984 at the University of Liège [38, 41, 42] and focused on the development of new constitutive laws at macroscale [43] or at microscale [44]. As demonstrated by Tuninetti et al. [18], the CPB06 yield locus can successfully predict the DH phenomenon exhibited by Ti6Al4V alloy for tensile and compressive loadings, and it addresses its strong evolving anisotropy behaviour. However, the high critical level of some Ti6Al4V applications along with its associated material high cost require accurate and reliable predictions of failure to optimize the design step [1, 45]. The model implemented in Lagamine in 2019 [18] did not involve damage prediction, and the current article addresses this limitation. Previous research outcomes presented in Refs. [3, 46, 47] show that fracture of Ti6Al4V at positive and high triaxialities is in fact driven by damage accumulation rather than plastic strain localization, evidencing the need of a validated damage accumulation and fracture prediction model. To this end, the SC11 damage law developed by Stewart & Cazacu [34] combining the flexible prediction capabilities of the CPB06 yield criterion and a damage law porosity ratio was implemented in Lagamine code. The single consideration of growth of voids as the only active damage mechanism in SC11 was subsequently expanded, considering growth, nucleation and coalescence of randomly distributed spherical voids like in [33]. It should be noted the latter article presented an application of an improved SC11 damage model of Ti6Al4V alloy recognising both the orthotropy of the material and the SD effect. This extended Stewart-Cazacu damage model (SC11−TN), includes damage mechanisms and follows the approaches developed by Tvergaard & Needleman [28]. According to Rojas-Ulloa et al. [33], satisfactory prediction results are achieved during small and mid-range deformations, whereas a loss of accuracy is reported during large tensile deformations by an overestimation of the material softening. This issue was attributed to the identification procedure of the damage law, which did not rely on an

accurate material hardening and could not determine the softening contribution. In this context, the current work presents a new contribution as the improved elastoplastic damage model is identified by a novel methodology. The implementation of the SC11−TNT damage law includes a Thomason-based coalescence criterion.

The article is organized as follows. Section 2 provides the theoretical formulation of the SC11−TNT law, its damage mechanisms as well as its integration scheme. Section 3 describes the investigated Ti6Al4V alloy including the performed experimental campaign and its numerical simulations. In addition, the method applied for the calibration of the elastoplastic and damage material parameters is presented. The numerical predictions of the implemented and identified damage model SC11−TNT are validated in section 4 by comparing them with experimental data. Finally, section 5 highlights the main conclusions of this work.

2. SC11−TNT micromechanics damage model

2.1. Formulation of the SC11−TNT damage law

The mathematical formulation is derived from the analytical solution of the deformation response of a spherical matrix material exhibiting orthotropic behaviour, SD effect, and containing randomly distributed spherical voids. The CPB06 yield stress [2, 6, 18, 48, 49], presented in Eq. (1), is used for describing the mechanical behaviour of the matrix material:

$$\bar{\Sigma}_{\mathrm{CPB06}} = \widetilde{m}\left\{\sum_{i=1}^{3}\left[(\Sigma_i - \mathbb{X}_i) - k|\Sigma_i - \mathbb{X}_i|\right]^a\right\}^{\frac{1}{a}} = \widetilde{m}F \tag{1}$$

where $\widetilde{m}$ is a constant that transforms the current CPB06 equivalent stress (F) into the material yield stress in the reference hardening direction ($\bar{\Sigma}_{\mathrm{CPB06}}$). Σ_i and $\mathbb{X}_i$ are respectively the eigenvalues of the corrected deviatoric stress and backstress tensors, k is the asymmetry parameter that accounts for the SD effect, and a is the homogeneity parameter. The corrected

stress ($\widehat{\mathbf{S}}$) and corrected backstress ($\widehat{\mathbf{X}}$) tensors are calculated by applying Eqs. (2) and (3) respectively:

$$\widehat{\mathrm{S}}_{ij} = L_{ijmn} T_{mnkl} \sigma_{kl} \tag{2}$$

$$\widehat{\mathrm{X}}_{ij} = L_{ijmn} T_{mnkl} X_{kl} \tag{3}$$

where L_{ijmn} is the 4th order orthotropic constants tensor, T_{mnkl} is the 4th order transformation tensor, σ_{kl} is the Cauchy stress tensor and X_{kl} is the backstress tensor.

The backstress tensor $\mathbf{X}$ is calculated using the model Armstrong-Frederick. This backstress model is given in its variational form in Eq. (4):

$$d\mathbf{X} = S_x [C_x d\boldsymbol{\epsilon}^p - \mathbf{X} d\bar{\epsilon}^p] \tag{4}$$

where S_x is the kinematic hardening saturation rate, C_x is the critical kinematic saturation value, $\boldsymbol{\epsilon}^p$ is the plastic strain tensor, and $\bar{\epsilon}^p$ is the equivalent plastic strain.

The 4th order orthotropic constant tensor, expressed in Voigt notation, is presented in Eq. 5.

$$\mathbf{L} = \begin{pmatrix} L_{11} & L_{12} & L_{13} & 0 & 0 & 0 \\ L_{12} & L_{22} & L_{23} & 0 & 0 & 0 \\ L_{13} & L_{23} & L_{33} & 0 & 0 & 0 \\ 0 & 0 & 0 & L_{44} & 0 & 0 \\ 0 & 0 & 0 & 0 & L_{55} & 0 \\ 0 & 0 & 0 & 0 & 0 & L_{66} \end{pmatrix} \tag{5}$$

The SC11–TNT micromechanics damage model is an extended version of the Stewart-Cazacu (SC11) damage law [34, 48]. For SC11, the function describing the yield of the material is obtained considering growth of voids as the only active damage mechanism, while further developments following a Gurson-type approach have resulted in the addition of nucleation and coalescence as damage mechanisms in [33]. The SC11–TNT damage law developed in in the current study considers growth, nucleation and coalescence of voids as damage mechanisms in addition with a Thomason-based coalescence criterion for in situ prediction of the onset of coalescence [50]. The analytical form of the SC11–TNT extended damage law is presented in Eq. (6):

$$\Phi(\boldsymbol{\sigma}, \mathbf{X}, \bar{\epsilon}^p) = \bar{\Sigma}_{\text{CPB06}} - \sigma_y (STF)^{\frac{1}{2}} = 0 \tag{6}$$

where $\boldsymbol{\sigma}$ is the Cauchy stress tensor, σ_y is the current yield stress of the material, and STF is the stress transformation function.

Grouping all the damage-related variables and parameters, STF is defined in Eq. (7):

$$STF = 1 - 2f^* q_1 \cosh\left[\frac{3q_2(\sigma_m - \mathrm{X}_m)}{h\sigma_y}\right] + q_3 f^{*2} \tag{7}$$

where f^* is the total porosity ratio considering the contributions of all currently active damage mechanisms, σ_m and X_m are the hydrostatic components of the corrected stress and backstress tensors respectively, h is the hydrostatic factor, and q_i (i=1,2,3) are parameters proposed by V. Tvergaard to improve numerical predictions [25, 28, 51]. The yield surface modification induced by the q_i parameters is intended to represent the effect of the interaction between voids. A thorough study on this subject was conducted by Ref.[52], where the optimal value of parameter q_1 was determined as $q_1 = 4e^{-1}$. Taking into consideration additional information on the application of similar Gurson-type models applied on this particular Ti-alloy [3, 34], the q_i parameters are hereafter fixed at $q_1 = 1.5$, $q_2 = 1.0$, and $q_3 = q_1^2$.

2.2. Implemented damage mechanisms and features

2.2.1. Nucleation

Nucleation of voids is defined as the onset of new microcavities within the porous matrix material. From a micromechanics perspective, this damage mechanism is observed around crystallographic instabilities such as the presence of inclusions or the interaction between crystals, as the decohesion of crystals and inclusions, as consequence of the continuous increment and localization of plastic deformations [19, 22, 24, 26, 28, 53]. The subsequent continuous increment of the porosity ratio attributed to these nucleated voids (also known as secondary voids) is mathematically modelled considering that the onset of cavities driven by local plastic deformations follows a statistical normal distribution [22, 24, 30, 33, 53]. The incremental form

of the model describing the continuous evolution of porosity ratio due to nucleation is presented in Eq. (8):

$$\dot{f}_n = \frac{F_N}{S_N\sqrt{2\pi}} \exp\left[-\frac{1}{2}\left(\frac{\bar{\epsilon}^p - \epsilon_N}{S_N}\right)^2\right] \dot{\bar{\epsilon}}^p \tag{8}$$

where $\dot{f}_n$ is the variational form of the porosity ratio amount attributed to nucleation, $\bar{\epsilon}^p$ is the equivalent plastic strain, $\dot{\bar{\epsilon}}^p$ the equivalent plastic strain rate, F_N the total nucleated porosity ratio of the material. S_N and ϵ_N are respectively the standard deviation and mean magnitudes for the normal distribution in terms of the equivalent plastic strain.

2.2.2. Growth

The growth of voids is defined as the volumetric enlargement of cavities contained within a porous material matrix as a consequence of the onset and increase of plastic deformations [11, 19–21, 23]. A simplified mathematical analysis of this phenomenon considering a small spherical void surrounded by an incompressible matrix material evidences a high relation between the growth of cavities and the volumetric part of the local radial velocity fields, while the change in shape of voids (i.e., ellipsoidal) is said to be related to the local tangent velocity fields [11, 20, 23, 27]. The mathematical void growth model used in this study was developed by A.L. Gurson [27] on the basis of the previously described mathematical approach. The incremental form of this void growth model is presented in Eq. (8):

$$\dot{f}_g = \sqrt{STF}\,\mathrm{tr}(\dot{\boldsymbol{\epsilon}}^p) \tag{9}$$

where $\dot{f}_g$ is the incremental form of the porosity ratio due to growth of voids, and $\mathrm{tr}(\dot{\boldsymbol{\epsilon}}^p)$ is the trace of the plastic strain rate tensor, representing the change rate of volume. Note that by neglecting the hyperbolic cosine function and assuming no effects of void-void interaction (i.e., q_i=1) in Eq.(7), the void growth formulation originally proposed by Gurson [27] is obtained from Eq. (9), where $\sqrt{STF} \approx (1 - f)$.

2.2.3. Coalescence

The coalescence is defined as the formation of larger cavities as consequence of the sudden phenomenon of fracture of the material found between voids. This damage mechanism is the result of the continuous increase in size and population of primary and secondary voids and of their interaction. This damage increase is related with the localization of the plastic flow [51, 53–61]. Coalescence is observed either as the pure plastic collapse of the material found in between voids, or as the formation of bridges or shear bands that eventually evolve into microcracks leading to the fracture of the material [3, 33, 53].

Following the Tvergaard and Needleman approach [28], the contribution of coalescence of voids in the total porosity ratio (f^*) is modelled in this study as a piecewise incremental function as seen in Eq. (10):

$$\dot{f}^* = \begin{cases} \dot{f} = \dot{f}_g + \dot{f}_n & for\ f \le f_{cr} \\ \left(\frac{\frac{1}{q_1} - f_{\mathrm{cr}}}{f_{\mathrm{F}} - f_{\mathrm{cr}}}\right)\dot{f} & for\ f > f_{cr} \end{cases} \tag{10}$$

where f_{cr} is the critical porosity ratio that determines the onset of coalescence, and f_{F} is the fracture porosity ratio [3, 28, 30, 33, 50, 53, 62]. The fraction $1/q_1$ represents the ultimate porosity ratio of the material.

To compute the growth and nucleation contributions in Eq. (10), both growth and nucleation of voids are considered as additive (i.e., $f = f_g + f_n$). The coalescence contribution to the total porosity ratio can be obtained by subtracting the growth and nucleation porosity ratio from the total porosity ratio (i.e., $f_c = f^* - f$).

2.2.4. Coalescence criterion

In ductile porous media undergoing large plastic deformations, the onset of coalescence (f_{cr}) is characterized as the moment when neighbouring cavities start to merge, forming large cavities and micro cracks that precede the fracture of the material. The prediction of the onset of

coalescence is then embedded in the mechanical analysis of the material found in between voids, and the determination of the moment when the load carrying capacity of these material bridges is lost [54]. Under this premise, the study of this phenomenon has looked at the development of reliable coalescence onset models for either coupled [50, 62–69] or non-coupled damage models (where a discrete damage indicator describing the local failure of the material is calculated [9]).

Knowing that the SC11—TNT damage law considers a macroscopic evolution of the porosity ratio without acknowledging size, shape or distribution of voids, in the current study the Thomason-based coalescence criterion developed by Zhang et al. [50] is implemented. This Thomason-Zhang criterion establishes the onset of coalescence as the moment when the inequality presented in Eq. (11) is no longer satisfied.

$$\frac{\sigma_1}{\sigma_y} \leq \frac{3}{2}\left[\alpha\left(\frac{1-\chi}{\chi}\right)^2 + \beta\chi^{-\frac{1}{2}}\right](1-\chi^2) \tag{11}$$

In Eq. (11), σ_1 is the first principal stress, χ is the ligament spacing ratio, while α and β are functions of the hardening exponent n of a J_2-type isotropic hardening law. Based on previous research results from Refs. [50, 64, 65], β = 1.24, whereas $\alpha(n) = 0.1 + 0.217n + 4.83n^2$. The coefficient n is calculated as the exponent of a J2-type isotropic hardening law. For this material, n=0.091616.

The ligament spacing ratio in a porous matrix material is related to the surface perpendicular to the local principal stress σ_1. It is defined as the ratio between solid (non-porous) and total (solid+porous) surface. Following the developments of Zhang et al.[50], χ is calculated as a function of the eigenvalues of the true strain tensor ($\epsilon_1 \geq \epsilon_2 \geq \epsilon_3$) and the total porosity ratio as seen in Eq. (12). The calculation of the strain tensor in our FE code Lagamine [38] is performed at a local level following a Lagrangian updated formulation, where the strain tensor is updated at each time step. The validity of the Lagrangian small strain approach used herein for calculating the true strain tensor within large deformations is corroborated in [70].

$$\chi = \frac{2\left[\left(\frac{3f^*}{4\pi}\right)\exp(\epsilon_1+\epsilon_2+\epsilon_3)\right]^{\frac{2}{3}}}{\sqrt{\exp(\epsilon_2+\epsilon_3)}} \quad (12)$$

2.2.5. Fracture propagation model

To provide a numerical insight into the effects of the local loss of load carrying capacity on the macro mechanical response of the material, a fracture initiation and propagation model is implemented in this study. A basic deleting element model (hereafter referred to as DELEM) is implemented within the SC11−TNT constitutive law in Lagamine FE code as a conditional routine to be activated when the element reaches a certain porosity ratio threshold (f_D^*). The element deleting process is modelled in the form of a gradual decrease of the stress in the element. This DELEM approach emulates the fracture propagation process by means of stress redistribution as nearby elements must now withstand the total load. The element is deleted when a value of $\sigma_{ij}=0$ is reached, resulting in a total loss of load carrying capacity in the element. The gradual decrement is set to occur within 4 seconds (simple regularization rule), a value that ensures a computational convergence while emulating what was experienced in laboratory conditions. The FE software Lagamine iterates until a total loss of convergence is achieved due to the numerical instability of the model as active elements are now unable to withstand the load.

2.3. Integration scheme

For the purpose of a more concise writing in the following equations of this section, the function describing the yield locus of the SC11−TNT damage law is hereafter defined as the subtraction of two functions as seen in Eq. (13):

$$\Phi(\boldsymbol{\sigma}, \mathbf{X}, \bar{\epsilon}^p) = \Phi_1(\boldsymbol{\sigma}, \mathbf{X}) - \Phi_2(\boldsymbol{\sigma}, \bar{\epsilon}^p) \leq 0 \quad (13)$$

where $\Phi_1 = \bar{\Sigma}_{\text{CPB06}}$ and $\Phi_2 = \sigma_y\sqrt{STF}$.

The flow rule of the constitutive law is defined in Eq. (14), where λ is the plastic corrector.

$$d\boldsymbol{\epsilon}^p = d\lambda\left(\frac{\partial\Phi}{\partial\boldsymbol{\sigma}}\right) \quad (14)$$

The presence of a stress-dependent hyperbolic cosine function within Φ_2 (see Eq. (7)) entails that the yield locus Φ is defined as a non-homogeneous function of the stress tensor $\boldsymbol{\sigma}$. The calculation of the associated flow rule (AFR) is therefore not trivial. The non-homogeneity of the function Φ is corroborated by applying the Euler homogeneous function theorem in Eq.(15). The derivative of the yield locus with respect to the stress tensor is presented in Appendix A.

$$\boldsymbol{\sigma}:\left(\frac{\partial\Phi}{\partial\boldsymbol{\sigma}}\right) \neq \boldsymbol{\sigma} \tag{15}$$

The correct formulation of the AFR is obtained by replacing Eq. (14) in the plastic work equivalence. Given the observation presented in Eq. (15), the equivalence between $d\bar{\epsilon}^p$ and $d\lambda$ must be corrected by a factor. The resultant AFR formulation is presented in Eq. (16),

$$d\bar{\epsilon}^p = d\lambda\left[\frac{\boldsymbol{\sigma}:\left(\frac{\partial\Phi}{\partial\boldsymbol{\sigma}}\right)}{\Phi_1}\right] = d\lambda\Lambda \tag{16}$$

where Λ is the variable representing hereafter the plastic multiplier corrector. The form of the AFR in Eq.(16) resembles that of a non-AFR formulation [71–73]. However, the plastic multiplied corrector in a strictly non-AFR formulation is a function of a plastic potential function: a plastic locus which has a different shape of the yield locus. Nevertheless, the effects of this AFR formulation onto the elastoplastic behaviour of the material are later assessed in section 4.

Let us consider the $(n+1)^{\text{th}}$ time step of the time integration scheme; the interval of which is described by $\Delta t_{n+1}=t_{n+1}-t_n$. A purely elastic behaviour of the material is initially assumed. Under this premise, a trial stress $\boldsymbol{\sigma}_{n+1}^{TRIAL} = \boldsymbol{\sigma}_n + \mathbb{C}^e\Delta\boldsymbol{\epsilon}_{n+1}$ is computed, where $\mathbb{C}^e$ is the elastic compliance matrix, $\boldsymbol{\sigma}_n$ is the stress tensor in the reference configuration, and $\Delta\boldsymbol{\epsilon}_{n+1}$ is the strain tensor in the incremental configuration. This first hypothesis is tested right away by calculating the magnitude of the damage law function from Eq. (13). If the evaluated yield function is found to be lower than or equal to zero, a completely elastic behaviour is confirmed, and all internal state variables are subsequently updated on this basis (i.e., $\boldsymbol{\sigma}_{n+1} = \boldsymbol{\sigma}_{n+1}^{TRIAL}$). However, if the result is greater than zero, an elastoplastic behaviour is assumed, and all the internal state variables in the incremented

configuration must be determined following a semi-implicit cutting plane algorithm [74]. This integration scheme is presented in Eqs. (17a) to (17f), defining the increments between configuration *n* and *n+1*

$$\Delta\boldsymbol{\epsilon}_{n+1} = \Delta\boldsymbol{\epsilon}^{e}_{n+1} + \Delta\boldsymbol{\epsilon}^{p}_{n+1} \tag{17a}$$

$$\Delta\boldsymbol{\epsilon}^{p}_{n+1} = \Delta\lambda_{n+1}\left(\frac{\partial\Phi}{\partial\boldsymbol{\sigma}}\right)_{n+1} \tag{17b}$$

$$\Delta\bar{\epsilon}^{p}_{n+1} = \Delta\lambda_{n+1}\Lambda_{n+1} \tag{17c}$$

$$\Delta\boldsymbol{\sigma}_{n+1} = \boldsymbol{\sigma}^{TRIAL}_{n+1} - \Delta\lambda_{n+1}\mathbb{C}^{e}\colon\left(\frac{\partial\Phi}{\partial\boldsymbol{\sigma}}\right)_{n+1} \tag{17d}$$

$$\Delta\mathbf{X}_{n} = C_{x}\left[S_{x}\Delta\lambda_{n+1}\left(\frac{\partial\Phi}{\partial\boldsymbol{\sigma}}\right)_{n+1} - \mathbf{X}_{n+1}\Delta\lambda_{n+1}\Lambda_{n+1}\right] \tag{17e}$$

$$\Phi\left(\boldsymbol{\sigma}_{n+1}, \mathbf{X}_{n+1}, \bar{\epsilon}^{p}_{n+1}\right) \leq \xi \tag{17f}$$

where ζ is the minimum acceptable error to be considered in the integration algorithm (ξ→0). The equation system presented here above is solved throughout the application of an iterative Newton-Raphson (N-R)-based algorithm [74]. Under this premise, a Taylor expansion of the damage law function is generated. The k^{th} iteration is presented in Eq. (18), where the objective value Φ^{k+1}_{n+1} is set to zero.

$$\Phi^{k+1}_{n+1} = \Phi^{k}_{n} + \left(\frac{\partial\Phi}{\partial\boldsymbol{\sigma}}\right)^{k}_{n+1}\colon\delta\boldsymbol{\sigma}^{k+1}_{n+1} + \left(\frac{\partial\Phi}{\partial\mathbf{X}}\right)^{k}_{n+1}\colon\delta\mathbf{X}^{k+1}_{n+1} + \left(\frac{\partial\Phi}{\partial\bar{\epsilon}^{p}}\right)^{k}_{n+1}(\delta\bar{\epsilon}^{p})^{k+1}_{n+1} = 0 \tag{18}$$

For the sake of a further concise writing of the mathematical formulation of the overall integration scheme, the partial derivatives are hereafter expressed as seen in Eqs.(19a)-(19d), while their respective analytical solutions are presented in Appendix A. Given that the backstress potential tensor is the mathematical representation of a tensor pointing towards the yield surface, it is computed as the opposite to the stress potential tensor as seen in Eq.(19b). Furthermore, as seen in Eq.(19d), the stress potential tensor in the $(k+1)^{\text{th}}$ iteration is hereafter

approximated as the stress potential in the previous k^{th} configuration, thus aiming for a more efficient computational procedure.

$$\left(\frac{\partial \Phi}{\partial \boldsymbol{\sigma}}\right)_{n+1}^{k} = \mathbf{Q}_{n+1}^{k} \tag{19a}$$

$$\left(\frac{\partial \Phi}{\partial \mathbf{X}}\right)_{n+1}^{k} \approx -\left(\frac{\partial \Phi}{\partial \boldsymbol{\sigma}}\right)_{n+1}^{k} = -\mathbf{Q}_{n+1}^{k} \tag{19b}$$

$$\left(\frac{\partial \Phi}{\partial \bar{\epsilon}^{p}}\right)_{n+1}^{k} = \mathrm{P}_{n+1}^{k} \tag{19c}$$

$$\left(\frac{\partial \Phi}{\partial \boldsymbol{\sigma}}\right)_{n+1}^{k+1} \approx \left(\frac{\partial \Phi}{\partial \boldsymbol{\sigma}}\right)_{n+1}^{k} \Longrightarrow \mathbf{Q}_{n+1}^{k+1} \approx \mathbf{Q}_{n+1}^{k} \tag{19d}$$

Taking into consideration Eqs.(19a)-(19d), the analytical calculation of the variational forms of the equivalent plastic strain, stress tensor, backstress tensor are presented respectively in Eqs. (20a)-(20c).

$$\delta \boldsymbol{\sigma}_{n+1}^{k+1} = -\delta \lambda_{n+1}^{k+1} \mathbb{C}^{e} : \mathbf{Q}_{n+1}^{k} \tag{20a}$$

$$\delta \mathbf{X}_{n+1}^{k+1} = \delta \lambda_{n+1}^{k+1} C_x \left[S_x \mathbf{Q}_{n+1}^{k} - \Lambda_{n+1}^{k} \mathbf{X}_{n+1}^{k} \right] \tag{20b}$$

$$\delta (\bar{\epsilon}^{p})_{n+1}^{k+1} = \delta \lambda_{n+1}^{k+1} \Lambda_{n+1}^{k} \tag{20c}$$

Taking into consideration the analytical resolution of the partial derivatives and the variational terms of Eqs. (19a)-(19d) and Eqs. (20a)-(20c) respectively, the final form of the N-R iterative algorithm is obtained from Eq.(18) by isolating the plastic multiplier in its variational configuration as a common variable within the terms of the equation. This final form is presented in Eq. (21).

$$\delta \lambda_{n+1}^{k+1} = \frac{\Phi_{n+1}^{k}}{\mathbf{Q}_{n+1}^{k} : \mathbb{C}^{e} : \mathbf{Q}_{n+1}^{k} + C_x \left[S_x \mathbf{Q}_{n+1}^{k} : \mathbf{Q}_{n+1}^{k} - \Lambda_{n+1}^{k} \mathbf{Q}_{n+1}^{k} : \mathbf{X}_{n+1}^{k} \right] - \mathrm{P}_{n+1}^{k} \Lambda_{n+1}^{k}} \tag{21}$$

All the state variables are updated at the end of each iteration, based on the determined magnitude of the plastic multiplier in its incremental configuration (see the analytical approach

of Eq.(20a)-(20c)). When the condition expressed in Eq.(17f) is met, the current state variables are considered correct and final for the particular $(n+1)^{th}$ time step. These state variables are subsequently used for calculating the elastoplastic compliance matrix by solving Eq. (23).

$$\mathbb{C}^{ep} = \mathbb{C}^{e} - \frac{(\mathbb{C}^{e}:\mathbf{Q})\otimes(\mathbb{C}^{e}:\mathbf{Q})}{\mathbf{Q}:\mathbb{C}^{e}:\mathbf{Q} - C_x[S_x\mathbf{Q}:\mathbf{Q} - \Lambda\mathbf{Q}:\mathbf{X}] - P\Lambda} \tag{22}$$

Finally, the strain tensor in the updated configuration is calculated as seen in Eq. (23) with the objective of further verification of the coalescence onset condition following the Thomason-Zhang criterion [50] reminded in Eqs. (11) and (12).

$$\boldsymbol{\epsilon}_{n+1} = \boldsymbol{\epsilon}_{n} + inv(\mathbb{C}^{ep})\Delta\boldsymbol{\sigma}_{n+1} \tag{23}$$

The overall integration algorithm can be summarized into a brief flowchart presented in **Fig. 1**.

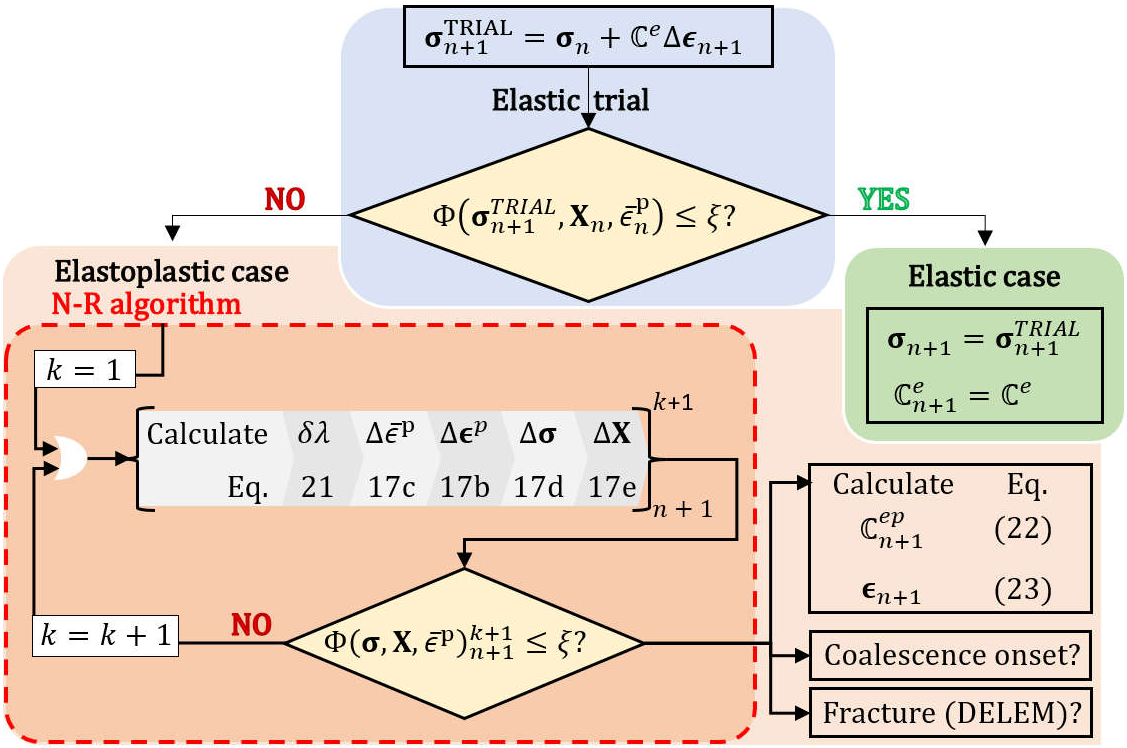

Fig. 1 Integration algorithm flowchart of SC11—TNT. ξ indicates a user-defined minimum admissible error for the N-R scheme. For this work, $\xi=1\times10^{-7}$.

3. Material and mechanical tests

3.1. Ti6Al4V titanium alloy

The tensile and compressive Ti6Al4V samples used in this study were originally obtained from a single batch of forged ingot samples. The orthogonal material directions are assigned in relation to the geometry of the original ingots as seen in **Fig. 2**, where the orthogonal direction triad (1,2,3) is defined as LD, TD and ST. The acronyms stand for longitudinal direction (LD), transversal direction (TD) and short transversal direction (ST).

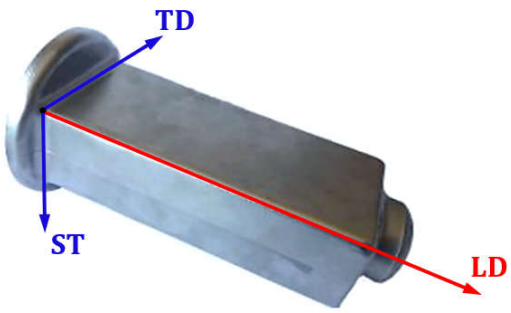

Fig. 2 Original Ti6Al4V ingot sample and material orthogonal reference frame.

In particular, LD axis (in red in **Fig. 2**) is the material reference direction where the hardening of the material is characterized. As in Refs. [5, 18, 75], the room temperature (RT) quasi-static plastic part of the reference stress-strain curve is modelled by the Voce hardening law (see Eq. (24)):

$$\sigma_y(\bar{\epsilon}^p) = \sigma_0 + S_R[1 - \exp(-C_R\bar{\epsilon}^p)] \tag{24}$$

where σ_0 is the initial yield stress, S_R is the saturation rate and C_R is the critical saturation rate of the material.

3.2. Mechanical tests

3.2.1. Experimental campaign

In order to correctly validate the numerical results, a wide range of stress triaxialities and distributions must be taken into consideration. Five cylindrical geometries with different circular cross section were tested in uniaxial tension and a compressive test was applied on an elliptic cylinder. The LD material direction is systematically the loading axis as shown in **Fig. 3**.

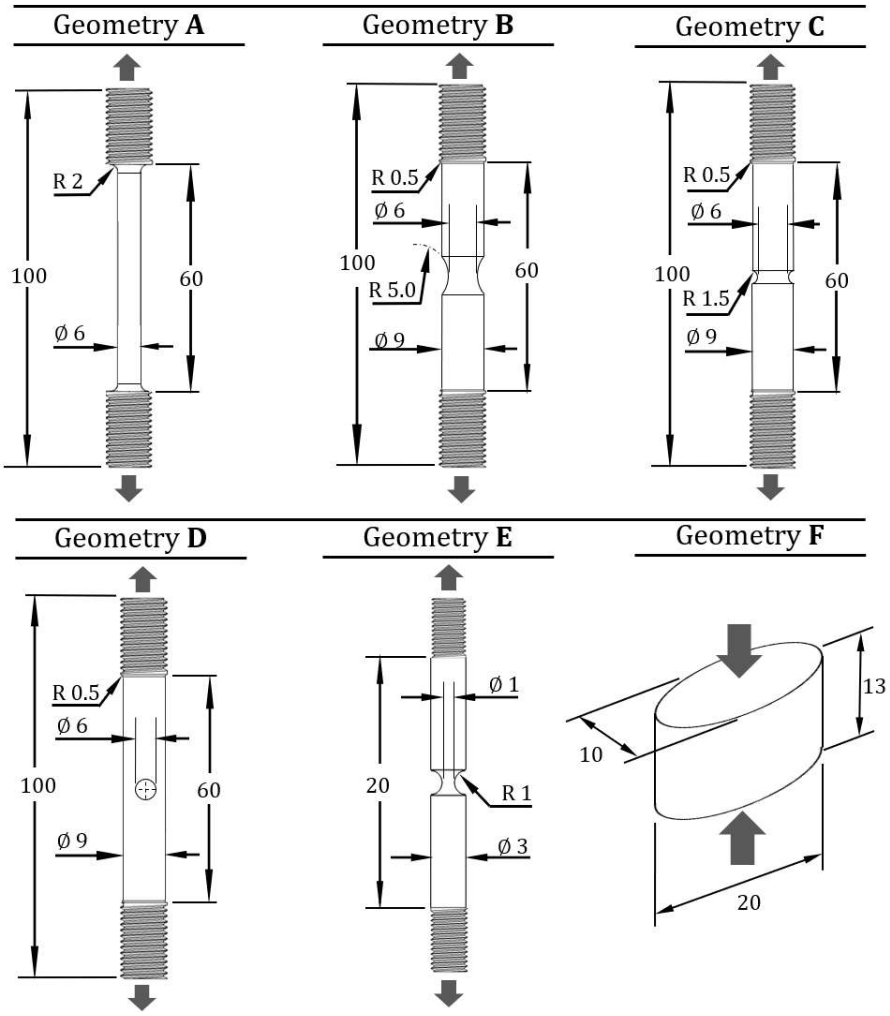

Fig. 3 Identification of the 6 test specimen geometries with dimensions in millimetres and applied loading.

Geometries A to E are submitted to quasi-static uniaxial and destructive tensile tests, whereas geometry F is submitted to a uniaxial non-destructive compressive test. The experimental tensile

tests were performed by Tuninetti et al. [18] on geometries A to D in the LD material direction and imposing a constant quasi-static strain rate of $\dot{\epsilon} = 1 \times 10^{-3}$ s^{-1} using a 100 kN electromechanical servo-hydraulic universal testing machine manufactured by Zwick. The axial displacement was continuously monitored by an extensometer with 40 mm gauge length, positioned at an initial equal distance of 20 mm from the central cross section of the tensile samples. The current shape and size of the cross section of the tensile samples were continuously monitored using a digital image correlation (DIC) system of 3 cameras that acquired reliable data of the necking start and longitudinal notch curvature of each specimen. These mechanical tests were repeated for each condition three times to provide an average force-displacement curve along with the respective standard deviations.

To obtain reliable in situ measurements of porosity ratio evolution in this titanium alloy, one in situ X-ray micro-tomography test was performed on geometry E, while a uniaxial quasi-static tensile test was ongoing. This experiment, performed by Lecarme et al. [47], consisted of the continuous tracking and measurement of cavities contained within a critical sub-volume located at the centre of the cross section of the notched.

Finally, a compressive test performed by Tuninetti et al. [5, 39] on geometry F is included within the test campaign to investigate large plastic compressive deformations. The experimental tests were performed at RT on a Schenk Hydroplus servo-hydraulic universal testing machine. The die displacement was constantly monitored in order to achieve a constant logarithmic strain rate of $\dot{\epsilon} = 1 \times 10^{-3}$ s^{-1} throughout continuous monitoring of the bulk sample deformation (for more information, please refer to Tuninetti et al. [6]). Due to the high risk of explosive fracture, this compressive test was not extended until the destruction of the specimen, thus avoiding harmful consequences for the team members and/or the machine itself.

3.2.2. Finite Element simulations

All further FE simulations are performed with Lagamine software [38]. To take advantage of the geometrical symmetry of the samples presented in **Fig. 3** across the axial and transversal planes, all the 3D FE simulations model one eighth of the total geometry. All the geometries were meshed using the GMSH software [76] and hexahedral "brick-like" elements with 8 nodes, 1 point of integration and 24 degrees of freedom (DOF) called BWD3D. This element adapted to large strains and large displacements is based on the non-linear three-field (stress, strain and displacement) HU-WASHIZU variational principle [77] .

The small geometry E is used to identify the damage set of parameters [33, 47]. It is modelled considering a minimum element edge size at the cross-section centre of 0.1 mm, enabling the damage analysis in line with experimental result accuracy. In order to perform local damage analyses without the need of a nonlocal damage approach [78, 79], for the larger samples, a single mesh size definition for geometries A, B, C and D is determined by executing a sensitivity analysis. A convergence analysis is performed using geometry B which develops large strains and a clear necking. Five different mesh densities (**Fig. 4(a)**) are assessed, considering a minimum element edge length at cross section ranging from 0.5 mm (with a total of 1 485 elements) up to 0.14 mm (with a total of 44 165 elements). Simulations are performed using the SC11—TN damage law, previously implemented and validated in Rojas-Ulloa et al. [33]. **Fig. 4(b)** shows the sensitivity analysis results in terms of maximum normalized force and maximum porosity ratio, for the damage set of parameters identified.

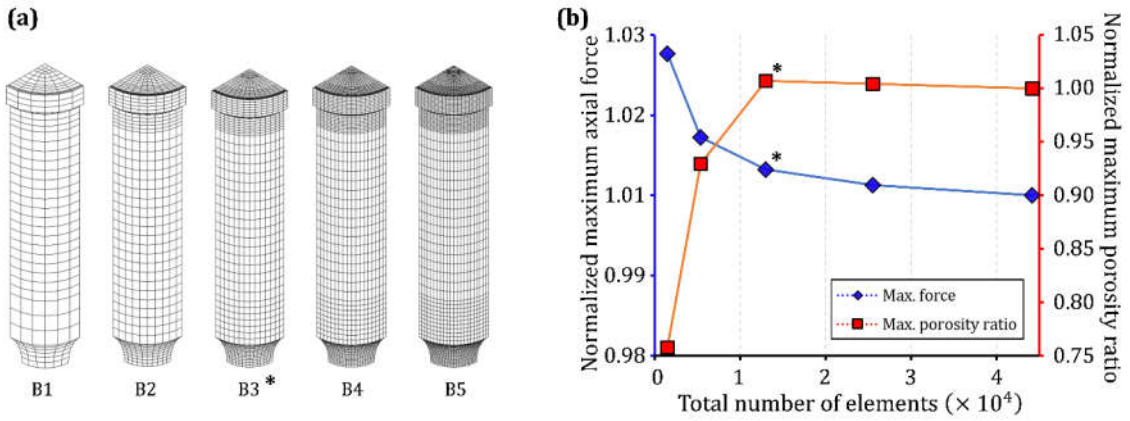

Fig. 4 (a) Mesh refinement of the convergence analysis **(b)** Variation of the maximum force and maximum porosity ratio for each mesh definition.

According to the results obtained from this mesh sensitivity analysis, the mesh B3 (marked with * in **Fig. 4**), with a minimum element edge length at the cross-section of 0.2 mm, is chosen as it exhibits a good balance between the computational efficiency and the local accuracy of numerical results.

The final meshes used for each geometry, their respective boundary fixations as well as the imposed displacements driving each simulation are presented in **Fig. 5**. The tensile tests are simulated, in a first stage, by imposing a constant axial displacement rate until reaching the maximum displacement experimentally measured without any delete element. In a second stage, simulations are performed for geometries A to D applying the DELEM approach able to follow crack propagation by a kill element approach, when a damage threshold value is reached.

The compression test (geometry F) is simulated by imposing a constant axial displacement rate of the plate punch located at the upper side of the modelled sample. The interface layer of contact elements CFI3D models the normal pressure and tangent friction stress applied on the sample by the punch. In Lagamine FE software, this element is based on a penalty approach and on a Coulomb contact friction law [80].

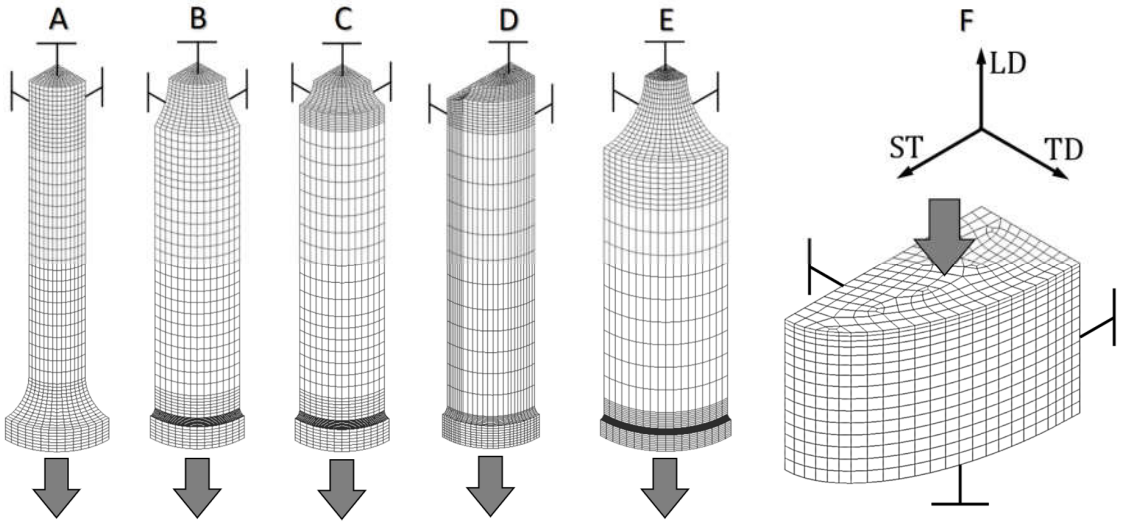

Fig. 5 Final meshes of each of the six geometry specimens (A to F) with their respective boundary conditions (arrows indicate an applied displacement, while ⊥ symbolizes no displacement condition in this plane).

3.2.3. Methodology of material parameter identification

The data set of the elastic parameters E_{ij}, the anisotropic parameters L_{ij}, a and SD parameter k for CPB06 law without damage were identified in a previous work ([5]. This identification methodology relied on monotonous uniaxial tensile tests in LT, TD, ST directions, shear tests and plane strain tests as well as compression tests performed with a full field displacement measurement by DIC. However, the measured stress-strain curve used to identify the hardening Voce parameters was limited to a medium strain 0.1. In [18], Tuninetti et al. identified the CPB06 law using larger strain range (until ε=0.2). Their application to the different tests (A, B, C, D, F geometries) proved that an improved identification of both SD parameter and Voce parameters could enhance the accuracy of the model predictions. The DH phenomenon was finally more accurately described by identifying 5 different yield surfaces at different plastic work levels. However as pointed by [18], all these previous attempts to model the Ti6Al4V behaviour did not address the material softening and the fracture modelling. This issue can be solved by the current

implementation of damage SC11—TNT law. In such case, a new set of hardening parameters and of course, the determination of the damage parameters is required.

In the presence of large plastic strains, porous ductile materials such as Ti6Al4V develop incremental and localized damage, however not in a continuous linear way. The damage increase affects the overall mechanical response of a specimen undergoing near-fracture tensile strains, causing a decrement of the load carrying capacity, observed as a negative slope in force-displacement curves (i.e., softening) [5, 18, 33]. While in the purely elastoplastic CPB06 yield criterion, the Ti6Al4V softening is only dependent on the isotropic hardening law and the necking phenomenon decreasing the section [5, 6, 18], the global softening behaviour predicted by the SC11−TNT coupled damage law depends on hardening, necking and material damage softening evolution. In this context, the identification of the damage-related parameters without any updating of the set of hardening parameters (data set of [33] used) has proven to be an incorrect approach, resulting in a huge overestimation of the material softening at fracture in Rojas-Ulloa et. al 's previous work [33]. In the current article, a sound methodology is applied. The identification of nucleation (F_N, S_N and ϵ_N) and coalescence (f_F) parameters in conjunction with the identification of a new set of parameters describing the hardening of the material (σ_0, S_R and C_R) is performed.

Before looking at the porosity increase, the initial porosity must be known. Using scanning electron microscopy (SEM) technique, Tuninetti et al. [18] reported an initial porosity ratio of $f_0 = 3 \times 10^{-5}$.

Nucleation parameter identification: the experimental data from an in situ X-ray micro tomography technique performed by L. Lecarme on a 1.0 mm Ti6Al4V notched bar (geometry E) undergoing a RT quasi-static tensile test [33, 47] are exploited. The continuum measurements of nucleated and total porosity ratio contained within a 0.2×0.2×0.2 mm^3 cubic sub-volume located at the centre of the cross-section of the tested specimen are achieved by applying a void tracking algorithm (see black-filled and black-hollow dot points in **Fig. 6**). The nucleation parameters (F_N

S_N and ϵ_N) are then identified following a purely damage-based inverse-analytical identification procedure relying on Eq. (8). The acquired nucleation contribution measurements of porosity are used to fit the numerical nucleation curve (see red dashed curve in **Fig. 6**).

Coalescence and hardening law parameters: Fixing the nucleation parameters found here above, the identification of the coalescence and the Voce isotropic hardening law parameters is performed by an inverse identification procedure based on two measured force-displacement curves. Indeed, to ensure an accurate prediction of the softening of the material along the entire elastoplastic range, both geometries A and B (see **Fig. 3**) are considered in the application of the automatic optimization algorithm OPTIM [81]. Based on the Levenberg-Marquardt algorithm, this home-made numerical module is able to simultaneously handle multiple experimental targets (tensile experiments of geometries A and B) and simulations. The root mean square percentile error between measurements and predictions is measured at the end of each iteration with a trial data set. The implemented algorithm is stopped when the numerical results obtained with the currently optimized set of material parameters is found within the error limits imposed by the user (ξ). A brief flowchart describing the application of this method is presented in **Fig. 7**.

In order to validate the new identified material data set reported in **Table 1**, a final tensile simulation of the geometry E (see **Fig. 3**) was performed. It allows quantifying the growth, nucleation and coalescence of voids using the optimized set of parameters. The numerically predicted void nucleation, growth and coalescence contained within the critical central element of the cross-section of this geometry are compared with the experimental data obtained in Refs. [47] as seen in **Fig. 6**

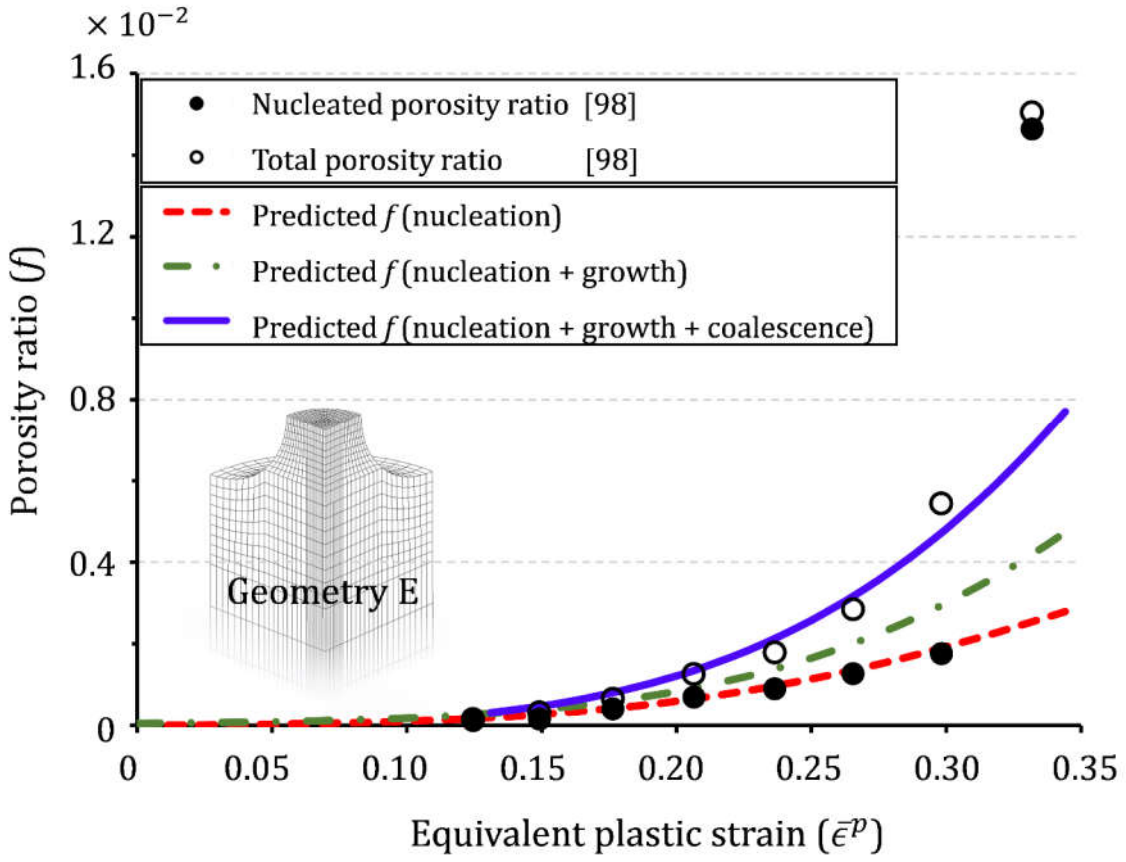

Fig. 6 Experimentally measured nucleated and total porosity ratio compared with the predicted porosity ratio at critical element of geometry E computed by a FE simulation with SC11—TNT law and data set of **Table 1**.

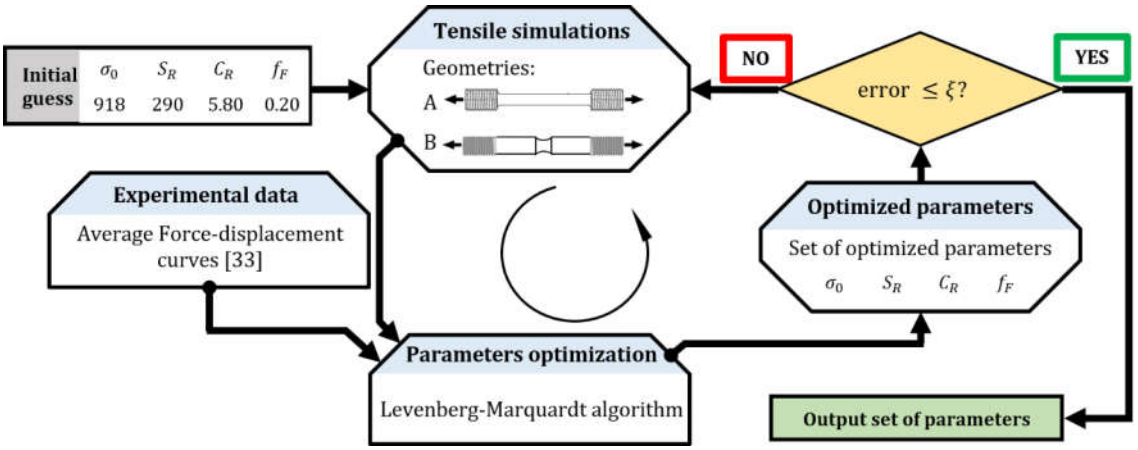

Fig. 7 Flowchart describing the identification procedure executed for finding the optimal coalescence and Voce's isotropic hardening law parameters.

Table 1. Final elastoplastic and damage related parameters for SC11—TNT.

Elastic constants [18]				
Test	E_{11} [MPa] / St.Dev.	E_{22} [MPa] / St.Dev.	E_{33} [MPa] / St.Dev.	$\upsilon_{12}= \upsilon_{13}= \upsilon_{23}$
Tension	111.0 ± 1	115.0 ± 4	117.0 ± 1	0.30
Compression	122.0 ± 1	128.0 ± 3	123.0 ± 3	0.30

Elastoplastic constants						
4^{th} order orthotropic constants matrix **L** [18]						
L_{11}	L_{12}	L_{13}	L_{22}	L_{23}	L_{33}	$L_{44} = L_{55} = L_{66}$
1.0	-2.373	-2.364	-1.838	1.196	-2.444	-3.607

Degree of homogeneity	Asymmetry parameter	Voce isotropic hardening parameters			
a	k	σ_0 [MPa]	S_R [MPa]	C_R	Ref.
2.0	-0.1361	918.0	290.0	5.80	[18]
		928.0	360.0	4.15	New data set for SC11—TNT

Damage parameters (new data set)

Initial porosity ratio	Fracture porosity ratio (see Eq. (10))	Nucleation parameters		
f_0	f_F	F_N	S_N	ϵ_N
3×10^{-5}	0.40	0.0070	0.130	0.380

As observed in **Fig. 6**, the optimized set of parameters provides an accurate quantification of damage accumulation in geometry E in comparison with the X-ray tomography experimental data from Refs. [47], however, a sudden divergence between experimental and numerical data is observed after reaching a total porosity ratio of $f^* \approx 5.0 \times 10^{-3}$. As discussed in Refs. [47, 82], this damage acceleration can be attributed to the interaction between voids which generates a rapid void growth, coalescence and formation of micro cracks. Within this first validation simulation, the DELEM fracture propagation approach is not activated as this module assumes crack event and no more porosity growth.

4. Results and validation of SC11—TNT

The validation of SC11—TNT damage law and its data set as well as the analysis of the results are given in this section. The damage distribution at fracture, the force-displacement curves, the cross-section evolutions for all the geometries are considered. The damage effect on the yield locus plots for different porosity values is also described and finally the crack propagation approach is discussed.

The magnitude and distribution of accumulated damage, triaxiality and plastic strain at the experimental rupture time using SC11–TNT with parameters with data set of **Table 1**, are presented in **Fig. 8** and in **Table 2**, for geometries A, B, C and D. The simulations are performed by imposing an axial displacement at a constant strain rate of 1×10^{-3} s^{-1} until the experimental fracture. As three samples were experimentally tested, the moment called “fracture” was arbitrary associated to the largest recorded displacement. As observed in **Fig. 8**, the fracture

onset for geometries A, B and D takes place in the centre of the cross-sections, whereas for geometry C, the fracture onset is located at the edge of the specimen cross section. As clearly seen in geometry C, and as it could be shown by a zoom for geometry B, the positions of the damage maximum do not correspond to the triaxiality ones in the cross sections of these specimens. This fact enhances the interest of an advanced model that involves in its damage indicator f^* numerous physical effects such as plastic strain, triaxiality, initial porosity, nucleation, and growth as well as a Thomason criterion to trigger coalescence event. A quantitative analysis of the results for the element exhibiting the maximum of damage f^* is presented in **Table 2**, pointing the different magnitudes of the integrated damage nucleation, growth, and coalescence porosity ratios. The geometries B, C, D show initial notched samples or holed specimen (**Fig. 3**). All these samples predict a maximum porosity ratio of the same magnitude order at rupture: 6-9 $\times 10^{-3}$. However, geometry A, a smooth bar sample (see **Fig. 3**) that due to necking finally present a small curvature (radius evolution from 6 mm to 4.5 mm) reaches a higher level of porosity ratio (5.3×10^{-2}) at fracture. This discrepancy generates an issue if one wants to select a threshold value of the damage factor to define a macro crack and delete finite elements. In the next simulations involving a basic crack propagation approach, two different fracture porosity ratios associated to a death element technique were used. For geometries B, C and D a threshold porosity ratio f_D^* value of 5×10^{-3} is used to start the delete element process while a f_D^*value of 4×10^{-2} was found to be suitable for geometry A. Such, different threshold values do not demonstrate a predictive facture approach. The reason of this issue can be attributed to the lack of gradient approach in the implemented damage model or the need of a different mesh density for geometry A in this simplified approach. The basic local approach used with a single length scale defined by the mesh size identified on B geometry (notched geometry) is representative of an approach that could be applied in an industrial context. The sensitivity to the simulation features of the elastoplastic simulation of a pure uniaxial test (without defect used to trigger necking) compared to the robustness of notched simulations is not surprising. Anyway, if this drawback for geometry A is

accepted, the current study confirms the model capacity to recover force-displacement curves **Fig. 9**, geometry evolutions **Fig. 10** and fracture events **Table 2**.

The axial force in FE simulations is directly obtained from the axial reaction of the nodes located at the symmetry cross section of the specimen. The correspondent axial displacements in tensile test simulations are measured in a plane located at an initial 20 mm distance from the cross section, thus emulating the position of the extensometer gauges during the experimental procedure. Note that for all the quasi-static experiments studied here, even for geometry A that does not force necking location, the fracture happens within this gauge zone and could be captured by a DIC system. By contrast, the displacement in the compressive test is measured from the displacement of the tool located on the upper surface of the bulk sample (for more information, please refer to Refs. [6, 18]).

Table 2. Computed local porosity ratio for each damage mechanism at fracture, maximum damage value and average initial and maximum final triaxiality at the cross-section.

Geometry	Maximum damage contributions of:			Maximum f^*	Average cross-section triaxiality at:	
	Growth	Nucleation	Coalescence		Initial stage	Final stage
A	2.49×10^{-2}	6.98×10^{-3}	2.12×10^{-2}	5.31×10^{-2}	0.33	0.93
B	1.55×10^{-3}	2.25×10^{-3}	2.28×10^{-3}	6.08×10^{-3}	0.50 ± 0.05	0.97
C	9.35×10^{-4}	2.80×10^{-3}	2.45×10^{-3}	6.18×10^{-3}	0.75 ± 0.05	1.33
D	2.47×10^{-3}	4.67×10^{-3}	2.48×10^{-3}	9.26×10^{-3}	0.50 ± 0.15	1.13

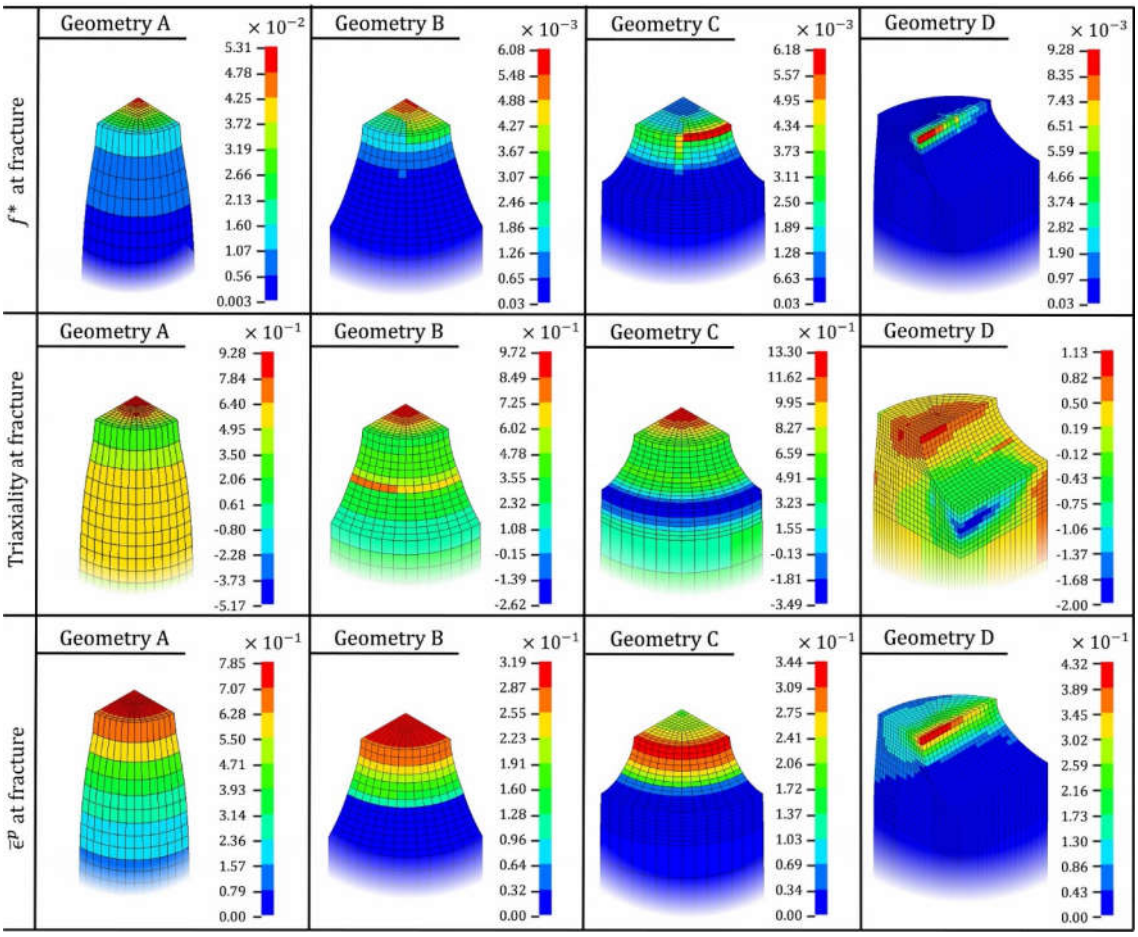

Fig. 8 Computed total porosity ratio f^*, triaxiality and plastic strain distribution at cross section of tensile test geometries A, B, C and D at final displacement stage (rupture) using SC11–TNT with damage.

The average-experimental and numerical force-displacement curves are presented and compared in **Fig. 9**. Note that the very small error vertical bars on the experimental curve enhances the very good repetition of the tests. The predictions of the simulations with CPB06 law (green curves) and its parameters determined in Ref. [18] are reminded in **Table 1** with the results of three applications of the new SC11–TNT damage law with different configurations. SC11—TNT simulations without damage (blue curves, $f^* = 0$) so similar to CPB06 case however with an increased hardening law defined in **Table 1** are presented. SC11—TNT simulations with damage (red curves, $f^* \geq f_0$) but no coupling with a crack propagation approach are also reported within, and finally the damage law coupled with DELEM module (orange curves). In **Fig. 9**, the

experimentally-observed fracture event is localised by two vertical lines at the end of the experimental force-displacement curves for geometries A, B, C and D. They identify the displacement of the first and the final fracture of the 3 experiments performed for each geometry. Moreover, note that no viscosity nor real analysis of the crack velocity were implemented in this implicit static elasto-plastic analysis. The model just aims to have an idea of the crack path. A real crack propagation model would require a dynamic approach and probably an explicit strategy to avoid convergence issues. The choice of decreasing the stress to null value in 4 seconds is a simple method to get convergence and visualize a possible crack propagation direction with the current available model.

Note that the curve ranking visible in the zoom images presents the expected order for geometries A, B, C. The blue curve (SC11—TNT without damage) is the highest as its hardening model provides the highest stress-strain curve (see **Table 1** for the Voce model parameters). When hardening is balanced by damage (red curve) a lower curve appears, which strongly softens while DELEM approach is activated (orange curve). The slope of the latter curve cannot be vertical as the crack propagation has not the correct speed as explained here above (Section 2.2.5); however, the fracture event it systematically identified in a correct manner.

About the geometry D, the ranking order between SC11—TNT results is kept, just the green curve of CPB06 law is now above. The hole geometry brings a totally different stress distribution and one cannot anymore associate the reaction force to roughly the integration of a uniaxial stress in vertical direction. Assuming a predominant vertical "uniaxial" stress component in the presence of hole of 6mm of diameter within a cylinder of 9 mm on diameter is here clearly not reasonable. So the fact that purely tensile CPB06 simulations (with lower Voce hardening data and considering textural hardening [18]) generate higher-above force-displacement curves in comparison with SC11—TNT (relying on higher hardening balanced or not by damage) evidences the complex distribution of stresses in this case and the impact of textural hardening and stress integration scheme.

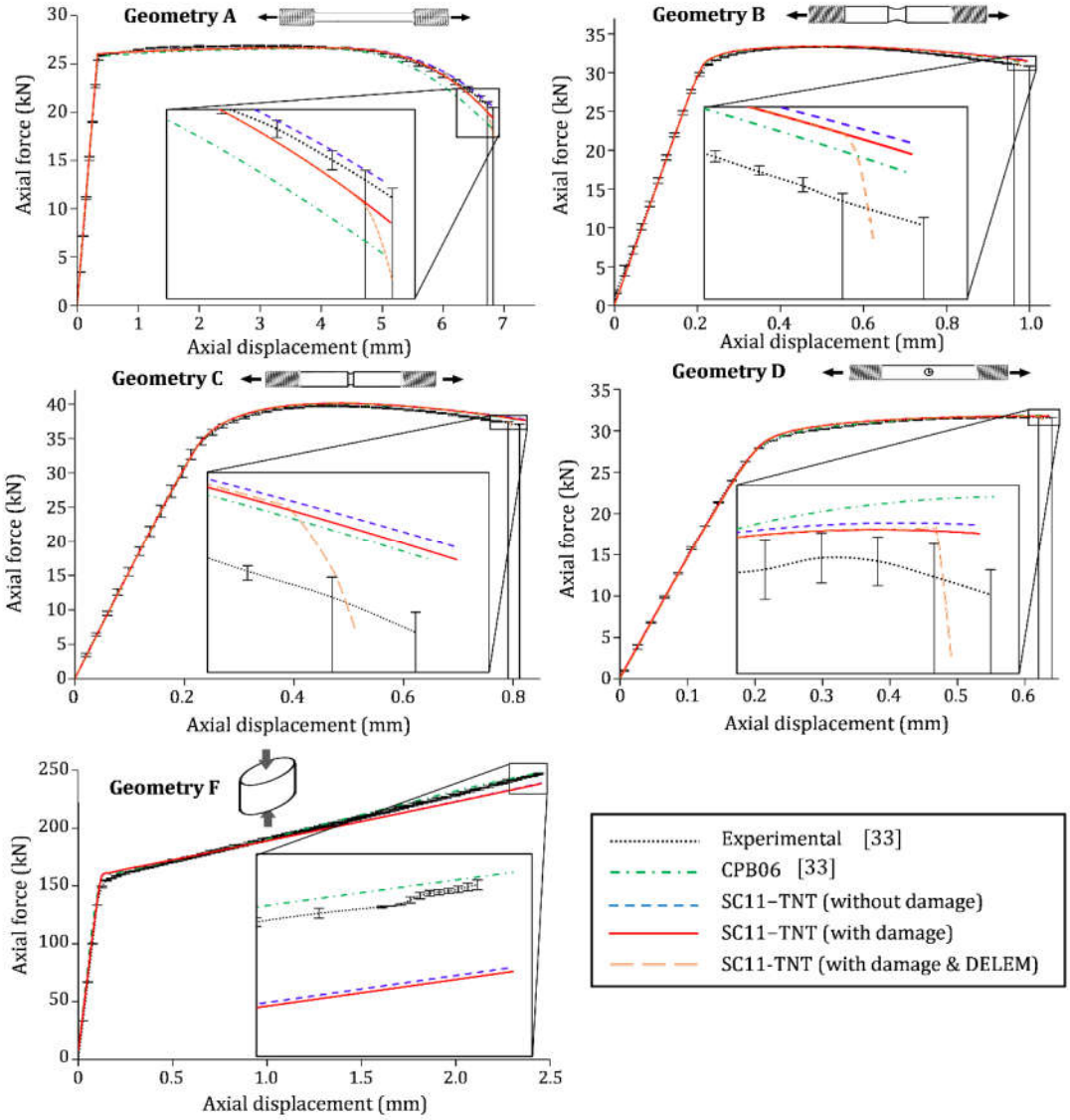

Fig. 9 Comparison of experimental and numerical force-displacement curves for tensile (geometries A to D) and for compression (geometry F) tests.

The compression case (geometry F) presents a low "damage" effect, since the initial porosity of voids healing by Eq. (9) has a poor effect, which is corroborated by the superposition of the blue and red curves. The barrelling phenomenon observed at large strains further enhances the

different behaviour exhibited by CPB06 and SC11—TNT, evidencing the effect of competition between textural hardening and amount of isotropic hardening and damage.

Fig. 10 shows the comparison of the predicted cross section diameter ratio (ST/TD) versus the in situ experimental measurements [18] for A, B, C, F geometries. All the blue and the red curves are nearly superimposed showing that the damage does not affect the anisotropic flow. This is not surprising as the porosity is assumed here spherical and does not affect the strength ratio between each direction.

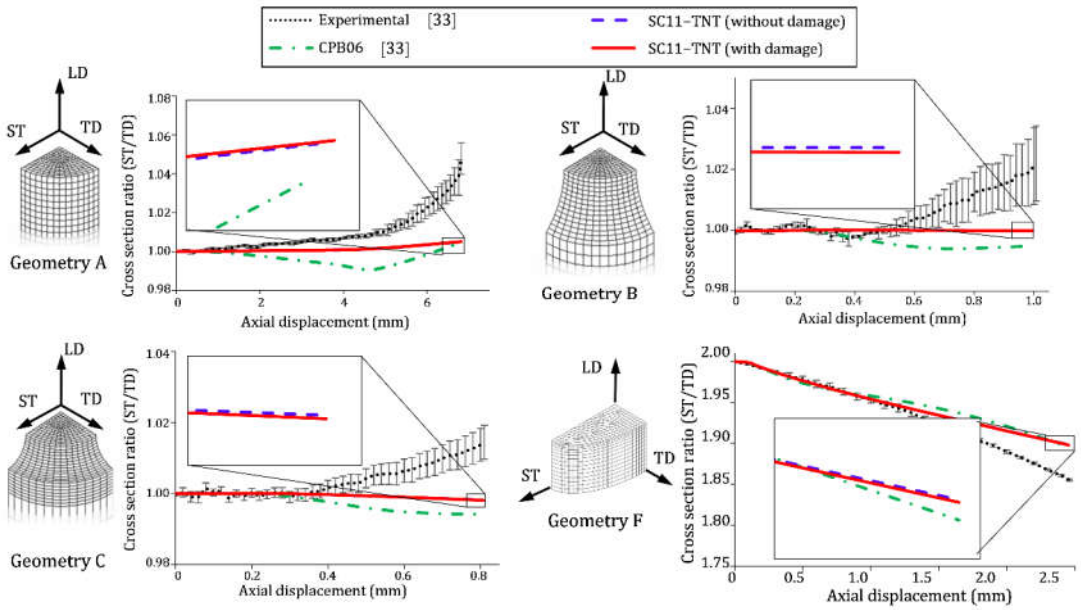

Fig. 10 Experimental and numerical cross-section shape deformation results for tensile (A, B, C) and compressive (F) test geometries.

In order to further analyse the coupled damage and plasticity interaction effect for this material, cuts within the orthotropic yield locus are presented in **Fig. 11** for both initial state and for a maximum plastic work of 206.6 J/cm^3), where both CPB06 [18] and SC11—TNT (with f^* of 5×10^{-3} and 4×10^{-2}) laws are evaluated.

The plots of **Fig. 11** assume a monotonic radial loading for each stress point. The results show that, as expected, the yield loci associated with the coupled damage SC11—TNT law decreases with increasing damage values. Furthermore, as damage accumulation does not affect the orthotropy of the material, or the DH effects, identical shapes are observed for any damage state. In contrast, the elastoplastic CPB06 yield criterion [18] presents an evolution of the cross-section shape yield locus identified by a series of 5 plastic work levels. This different hardening approach could explain the less monotonous evolution of the sample shapes based on CPB06 simulations observed in **Fig. 10** as well as the ranking of Force-Displacement curves in **Fig. 9**. The complexity of CPB06 hardening model is however increased as well as its identification.

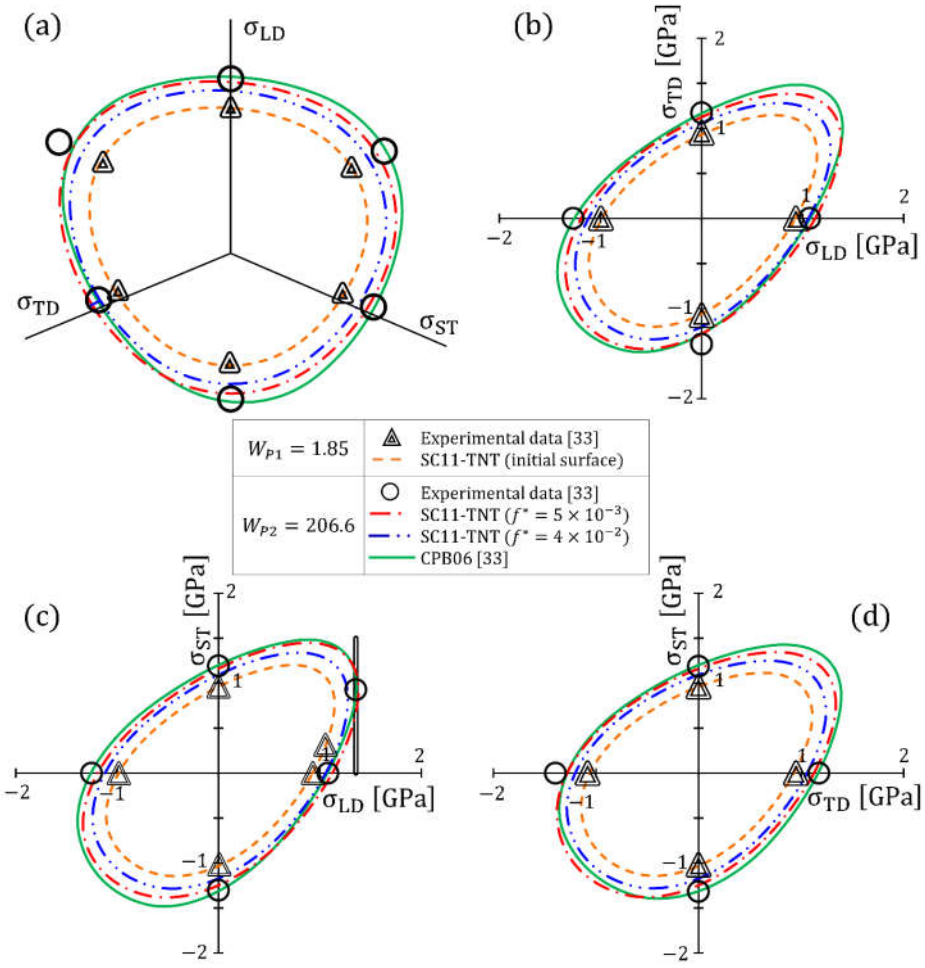

Fig. 11 Yield locus for SC11–TNT damage law for Ti6Al4V evaluated for the initial state (Wp_1= 1.85 J/cm^3) and at a 2nd plastic work Wp_2=206.6 J/cm^3 considering SC11—TNT at different f^*

magnitudes (5×10^{-3} and 4×10^{-2}) and CPB06 from [18]; (a) π-plane; (b) σ_{LD}-σ_{TD} plane; (c) σ_{LD}-σ_{ST} plane; (d) σ_{TD}-σ_{ST} plane.

Finally, the coalescence criterion implemented in SC11—TNT aims to predict the collapse of the material found between voids as function of the stress state and the distribution, size and shape of voids. According to the theoretical model basis, this is achieved by predicting the loss of the load carrying capacity of material bridges found in-between ideally equispaced voids undergoing shape changes and size increments as the plastic strain increases. In reality however, the primary and secondary void populations often exhibit wide variations in terms of distribution, size and shape. Furthermore, the complex microstructure of this Ti-alloy (in particular, the lamellar α/β interfaces) [2, 7] has reportedly favoured the formation of extremely irregular cavities [47]. Consequently, finding a reliable approach able of delivering statistically accurate results is difficult to achieve.

The Thomason-Zhang coalescence extension [54] implemented in the SC11−TNT is formulated following an initially standard Thomason formulation, however the evolution of the void size, shape and spatial arrangement is determined from the total porosity ratio f^* and the strain tensor. This choice induces a reliable and computationally efficient macroscopic depiction of the coalescence onset [69, 83]. Furthermore, the damage evolution related to the progressive increment in the threshold value f_{cr} defining the coalescence start results in a steeper localization of the accumulated damage, often exhibiting an anisotropic distribution. This choice affects the critical locations where the fractures caused by excessive damage accumulation are expected to start. In **Fig. 12**, the distribution of the damage mechanisms within the tensile samples of geometries A to D at maximum displacement (no DELEM) is shown in the first line while the second line shows the final fracture propagation results obtained by applying the DELEM approach.

The decreased load carrying capacity of the sample caused by the fracture modelled by the red elements deleted from the mesh, is found within a remarkably good agreement with the experimentally predicted fracture of the samples (**Fig. 12** and **Fig. 9**).

From a microscopic point of view, in-situ fracture porosity ratio measurements could confirm the numerically predicted f_D^* (see **Table 2**) for this batch of Ti6Al4V. The porosity ratio measurements performed via an in-situ X-ray microtomography at UCLouvain (see [47] and Fig. 6) provide a valuable depiction of the damage evolution within the first stages. However, the subsequent coalescence-nucleated void recognition failure of the void tracking algorithm results in unreliable porosity ratio measurements at fracture. In Ref. [33] working on the same material batch at Universidad de La Frontera and ULiège (UFRO-ULiège), a porosity ratio analysis was performed throughout post processing of scanning electron microscope (SEM) images obtained from a 2.5 mm notched bar submitted to a loading that was stopped near the fracture tensile state. The measured average near-fracture porosity ratio was $f^*=5.5 \times 10^{-3} \pm 0.004$. Extensive damage-oriented experimental Ti6Al4V campaigns were also performed by Ghent University (UGent) in [3]. These researchers post processed SEM images obtained from fractured sheet and cylindrical tensile samples. In quasi-static tensile tests performed on sheets, an average porosity ratio of $f^* \approx 5.0 \times 10^{-3}$ was found within the first 100 μm zone from the fracture location, whereas a similar analysis performed on a round tensile bar (similar to geometry A) exhibited a porosity ratio up to $f^* = 2.0 \times 10^{-2}$. Experimental results from ULiège, UFRO and UGent indicate that porosity amount at fracture strongly varies according to the stress state.

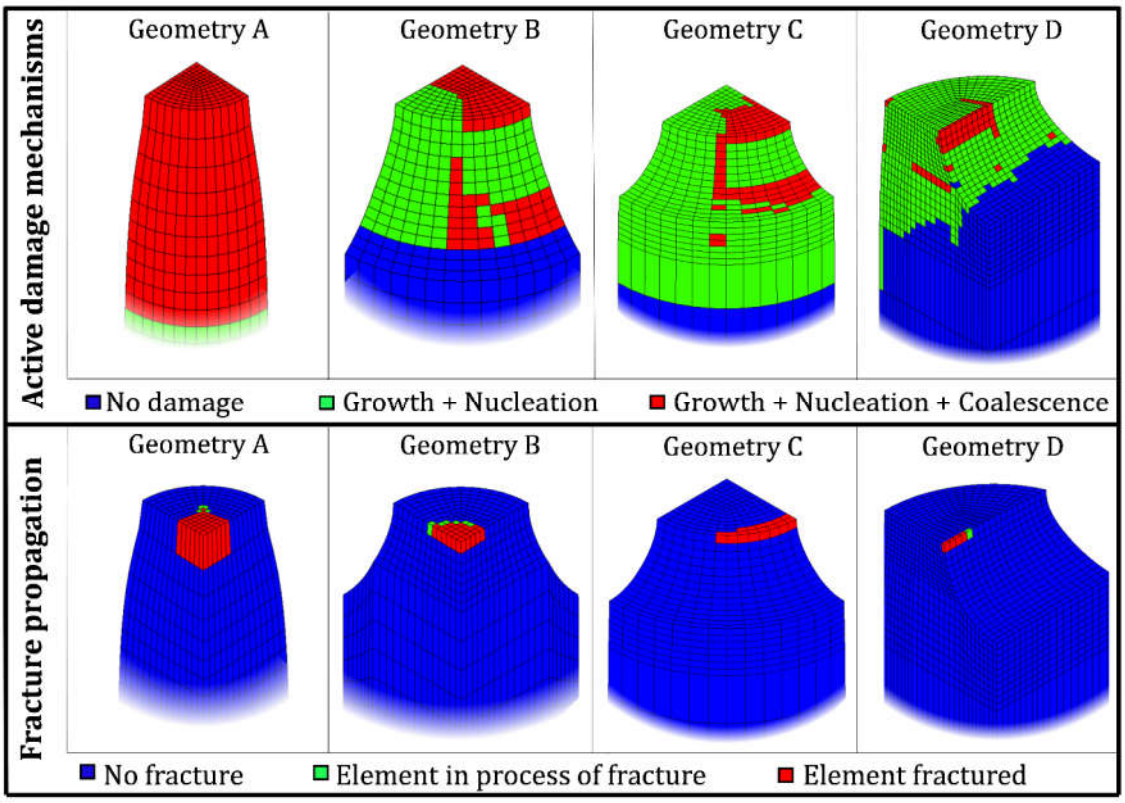

Fig. 12 Predicted distribution of active damage mechanisms at fracture computed by SC11-TNT and crack propagation according DELEM activated module.

The numerically identified fracture porosity ratio for DELEM (f_D^*= 5 × 10^{-3}) applied in geometries B, C and D is found in very good agreement with the UGent [3] and ULiège experimental findings, also close to 5 × 10^{-3}, whereas an overestimation of the computed f_D^* value (5.31 × 10^{-2}) seems present in geometry A measured by UCLouvain (see **Table 2**). However, this higher value is closed from the value also identified in [3] for uniaxial tensile tests on cylinders. UGent researchers [3] attribute the particularly high porosity ratio in smooth cylindrical specimens to the nearly pure tensile stress state, that results in a delayed onset of coalescence allowing large damage increments prior to the onset of coalescence, micro cracks and fracture. Based on these experimental observations, it is possible to better understand the damage threshold value f_D^* numerically found by inverse modelling. A more advanced model paying a stronger attention to void shape in pure tensile tests could be closer from the physics for the accurate prediction of coalescence.

5. Conclusions

An anisotropic coupled damage-elasto-plastic model describing strength differential effect, void growth, nucleation and coalescence damage mechanisms was successfully implemented in the FE software Lagamine. The implemented SC11−TNT model is coupled to a Thomason-based criterion to determine the onset of coalescence. Applied on the ductile fracture of Ti6Al4V, the model is validated for 6 different test geometries covering triaxiality variations from 0.33 (initial tensile state) to 1.13 (final state of a notched specimen with 1.5 mm radius). The choice of a single mesh density for all samples compensated the lack of non-local implementation. A rough method of kill element gives the trend of crack propagation.

After analysing the results, the authors state that:

- The joint identification of the coalescence parameter (f_F fracture porosity ratio, defining the numerical evolution of f^* during coalescence event) and of the Voce isotropic hardening parameters based on a Levenberg-Marquart optimization algorithm proved to be highly reliable, obtaining a parameter data able to identify both the fracture moment and location for different loading cases.
- The inclusion of the Thomason-based coalescence onset criterion within the SC11−TNT coupled damage law enhances the localization of the damage. Depending on the geometry, a strong anisotropic damage distribution in the cross section of the specimens can appear. The numerical model provides the respective ratios between nucleated, growth and coalescence porosity fractions.
- The threshold porosity value f_D^* defining the crack event is numerically identified on different geometries and consistent with the current experimental observations, as well as the measurements found in the literature.
- The mathematical formulation of the associated flow rule is for this coupled damage law a non-trivial case. Due to the stress inhomogeneity exhibited by the yield function, a

plastic multiplier corrector is included within the associated flow rule in a similar manner to that of a non-associated formulation. This approach differs from a non-associated flow rule because of the use of the same yield function (i.e., no new plastic potential function was defined). As a result, only the diagonal components of the vector defining the direction of plastic deformations normal to the yield surface are affected. This entails a change in the projected size of the yield surface, without affecting its shape.

The SC11—TNT model presented in this work has been validated for a variety of positive triaxialities in order to ascertain its capabilities. It provides a solid foundation for any further extensions of the model. For instance, the Armstrong Frederic kinematic hardening law is included within the yield stress definition of the implemented SC11—TNT, allowing the modelling of damage accumulation during cyclic loadings. However, this phenomenon is not present within the simulated tests of the current article. A future work will consist of the use of experimental data on the Bauschinger effect for an extended validation of this law feature. A non-local SC11-TNT version incorporating the significant effect of gradients, shear damage extensions and textural hardening are also of current interest.

CRediT authorship contribution statement

Carlos Rojas-Ulloa: Data curation, Software, Investigation, Formal analysis, Validation, Writing – original draft. **Víctor Tuninetti:** Conceptualization, Formal analysis, Investigation, Funding acquisition, Methodology, Supervision, Writing - review & editing, Project administration. **Héctor Sepúlveda**: Investigation, Data curation. **Ehssen Bettaieb**: Software, Data curation. **Gonzalo Pincheira:** Formal analysis, Writing - review & editing. **Gaëtan Gilles**: Software, Data curation. **Laurent Duchêne:** Methodology, Writing - review & editing. **Anne Marie Habraken**: Conceptualization, Formal analysis, Funding acquisition, Methodology, Supervision, Writing - review & editing, Project administration.

Acknowledgements

This work was funded by the international cooperation agreement WBI/AGCID SUB2019/419031 (DIE19-0005) and the international collaborative research project WBI/AGCID RI02 (DIE23-0001), the Universidad de La Frontera Internal Research Fund DIUFRO (Project DI22-0067) and FRIA Grant N°4000-8987 (F.R.S.-FNRS., Belgium). As research director of F.R.S.-FNRS, A.M.H. thanks the Fund for Scientific Research for financial support. The authors also acknowledge the Dirección de Investigación (Universidad de La Frontera) for partial funding, the FONDEQUIP EQM130014 and EQM180111.

Appendix A. Analytical expressions of SC11−TNT damage law partial derivatives for integration scheme

In this section, the partial derivatives of the SC11−TNT damage law function with respect to the Cauchy stress tensor and with respect to the equivalent plastic strain (**Q** and P respectively, as named in Section 2.3) are analytically calculated. With the aim of generating concise mathematical expressions, the form of the SC11−TNT damage law function is hereafter expressed as seen in Eq. (A.1), where $\phi_1 = \bar{\Sigma}_{\text{CPB06}}$ and $\phi_2 = \sigma_y\sqrt{STF}$.

$$\Phi(\boldsymbol{\sigma}, \mathbf{X}, \bar{\epsilon}^p) = \phi_1(\boldsymbol{\sigma}, \mathbf{X}) - \phi_2(\boldsymbol{\sigma}, \mathbf{X}, \bar{\epsilon}^p) \tag{A.1}$$

The partial derivative of the SC11—TNT damage law function with respect to the Cauchy stress tensor is then expressed as:

$$\frac{\partial \Phi}{\partial \boldsymbol{\sigma}} = \frac{\partial \phi_1}{\partial \boldsymbol{\sigma}} - \frac{\partial \phi_2}{\partial \boldsymbol{\sigma}} \tag{A.2}$$

The first partial derivative term from Eq. (A.2) must be decomposed following the so-called chain rule of calculus. The second partial derivative of Eq. (A.2) is directly obtained by performing a single-step derivation. The solutions for the first and second partial derivative terms are respectively presented in Eqs. (A.3a) and (A.3b), where **I** is the 2nd order identity tensor.

$$\frac{\partial \phi_1}{\partial \boldsymbol{\sigma}} = \sum_{i=1}^{3} \frac{\partial \phi_1}{\partial \Sigma_i} \frac{\partial \Sigma_i}{\partial \hat{\mathbf{S}}} \frac{\partial \hat{\mathbf{S}}}{\partial \boldsymbol{\sigma}} \tag{A.3a}$$

$$\frac{\partial \phi_2}{\partial \boldsymbol{\sigma}} = \frac{-q_1 q_2 f^*}{h\sqrt{STF}} \sinh\left[\frac{3q_2(\sigma_m - \mathrm{X}_m)}{h\sigma_y}\right] \mathbf{I} \tag{A.3b}$$

Finally, the analytical resolution of the three partial derivatives from Eq. (A.3a) are resented in Eqs. (A.4a)-(A.4c) respectively.

$$\frac{\partial \phi_1}{\partial \Sigma_i} = \widetilde{m}\left[F^{\left(\frac{1}{a}-1\right)}\right]\left\{\sum_{i=1}^{3}[(\Sigma_i - \mathbb{X}_i) - k|\Sigma_i - \mathbb{X}_i|]^{a-1}\right\}[sign(\Sigma_i) - k] \tag{A.4a}$$

$$\frac{\partial \Sigma_i}{\partial \hat{\mathbf{S}}} = \begin{cases} \frac{1}{3\Sigma_i^2 - 2\mathrm{I}_1\Sigma_i + \mathrm{I}_2}\left(\Sigma_i^2 \frac{\partial \mathrm{I}_1}{\partial \hat{\mathbf{S}}} - \Sigma_i \frac{\partial \mathrm{I}_2}{\partial \hat{\mathbf{S}}} + \frac{\partial \mathrm{I}_3}{\partial \hat{\mathbf{S}}}\right) & if\ 3\Sigma_i^2 - 2\mathrm{I}_1\Sigma_i + \mathrm{I}_2 \neq 0 \\ \frac{1}{6\Sigma_i^2 - 2\mathrm{I}_1\Sigma_i}\left(\Sigma_i^2 \frac{\partial \mathrm{I}_1}{\partial \hat{\mathbf{S}}} - \Sigma_i \frac{\partial \mathrm{I}_3}{\partial \hat{\mathbf{S}}}\right) & otherwise \end{cases} \quad \text{(A.4b)}$$

$$\frac{\partial \hat{\mathbf{S}}}{\partial \boldsymbol{\sigma}} = \mathbf{LT} \quad \text{(A.4c)}$$

Particularly in Eq. (A.4b), the partial derivative of the corrected stress eigenvalues Σ_i with respect to the corrected deviatoric stress tensor $\hat{\mathbf{S}}$ is calculated as function of the invariants (I_1, I_2, I_3) and eigenvalues ($\Sigma_1 \geq \Sigma_2 \geq \Sigma_3$) of $\hat{\mathbf{S}}$, so that the condition expressed by the characteristic polynomial is fulfilled $\Sigma_i^3 - \mathrm{I}_1\Sigma_i^2 + \mathrm{I}_2\Sigma_i + \mathrm{I}_3 = 0$.

Following the approach proposed in Eq. (A.1), the partial derivative of the SC11–TNT damage law function with respect to the equivalent plastic strain ($\bar{\epsilon}^p$) is presented in Eq. (A.5).

$$\frac{\partial \Phi}{\partial \bar{\epsilon}^p} = \frac{\partial \phi_1}{\partial \bar{\epsilon}^p} - \frac{\partial \phi_2}{\partial \bar{\epsilon}^p} \quad \text{(A.5)}$$

The partial derivative of ϕ_1 from Eq. (A.5) is zero as there is no explicit dependence on the equivalent plastic strain. The partial derivative of the partial derivative of ϕ_2 is presented in Eq. (A.6).

$$\frac{\partial \phi_2}{\partial \bar{\epsilon}^p} = \frac{\partial \sigma_y}{\partial \bar{\epsilon}^p}\sqrt{STF} + \frac{\sigma_y}{2\sqrt{STF}}\left\{-2q_1\left[\frac{\partial f^*}{\partial \bar{\epsilon}^p}\cosh\left(\frac{3q_2(\sigma_m - \mathrm{X}_m)}{h\sigma_y}\right) - f^*\sinh\left(\frac{3q_2(\sigma_m - \mathrm{X}_m)}{h\sigma_y}\right)\frac{3q_2(\sigma_m - \mathrm{X}_m)}{h\sigma_y^2}\frac{\partial \sigma_y}{\partial \bar{\epsilon}^p}\right] + 2q_3 f^* \frac{\partial f^*}{\partial \bar{\epsilon}^p}\right\} \quad \text{(A.6)}$$

The partial derivatives of the yield stress and the total porosity ratio *f** are analytically solved in Eq. (A.7) and **Table A.1** respectively. In particular, the derivative of *f** with respect to the equivalent plastic strain is defined in relation to the currently active damage mechanisms defined by the user and activated within the FE software.

$$\frac{\partial \sigma_y}{\partial \bar{\epsilon}^p} = S_{\mathrm{R}} C_{\mathrm{R}} \exp(-C_{\mathrm{R}} \bar{\epsilon}^p) \quad \text{(A.7)}$$

Table A.1: Analytical definition of total porosity ratio derivatives in relation to the currently active damage mechanisms.

No active damage mechanisms	
$\frac{\partial f^*}{\partial \bar{\epsilon}^p} = 0$	(A.8a)
Active damage mechanisms: Growth voids	
$\frac{\partial f^*}{\partial \bar{\epsilon}^p} = \frac{\partial f_g}{\partial \bar{\epsilon}^p} = \frac{\sqrt{STF}}{\Lambda} \mathrm{tr}\left(\frac{\partial \Phi}{\partial \boldsymbol{\sigma}}\right)$	(A.8b)
Active damage mechanisms: Growth and nucleation of voids	
$\frac{\partial f^*}{\partial \bar{\epsilon}^p} = \frac{\partial f_g}{\partial \bar{\epsilon}^p} + \frac{\partial f_n}{\partial \bar{\epsilon}^p} = \frac{\sqrt{STF}}{\Lambda} \mathrm{tr}\left(\frac{\partial \Phi}{\partial \boldsymbol{\sigma}}\right) + \frac{F_\mathrm{N}}{S_\mathrm{N}\sqrt{2\pi}} \exp\left[-\frac{1}{2}\left(\frac{\bar{\epsilon}^p - \epsilon_\mathrm{N}}{S_\mathrm{N}}\right)^2\right]$	(A.8c)
Active damage mechanisms: Growth, nucleation, and coalescence of voids	
$\frac{\partial f^*}{\partial \bar{\epsilon}^p} = \begin{cases} \frac{\partial f_g}{\partial \bar{\epsilon}^p} + \frac{\partial f_n}{\partial \bar{\epsilon}^p} = \frac{\sqrt{STF}}{\Lambda} \mathrm{tr}\left(\frac{\partial \Phi}{\partial \boldsymbol{\sigma}}\right) + \frac{F_\mathrm{N}}{S_\mathrm{N}\sqrt{2\pi}} \exp\left[-\frac{1}{2}\left(\frac{\bar{\epsilon}^p - \epsilon_\mathrm{N}}{S_\mathrm{N}}\right)^2\right] & \text{If coalescence is not active} \\ \left(\frac{\frac{1}{q_1} - f_{cr}}{f_F - f_{cr}}\right)\left\{\frac{\sqrt{STF}}{\Lambda} \mathrm{tr}\left(\frac{\partial \Phi}{\partial \boldsymbol{\sigma}}\right) + \frac{F_\mathrm{N}}{S_\mathrm{N}\sqrt{2\pi}} \exp\left[-\frac{1}{2}\left(\frac{\bar{\epsilon}^p - \epsilon_\mathrm{N}}{S_\mathrm{N}}\right)^2\right]\right\} & \text{Otherwise} \end{cases}$	(A.8d)

References

1. Cecchel S, Ferrario D, Mega F, Cornacchia G (2021) Numerical, Mechanical, and Metallurgical Investigation of an Innovative Near Net Shape Titanium Selective Laser Melting Engine Component and Comparison with the Conventional Forged One. Adv Eng Mater 23:1–10. https://doi.org/10.1002/adem.202100036

2. Tuninetti V, Jaramillo AF, Riu G, et al (2021) Experimental Correlation of Mechanical Properties of the Ti-6Al-4V Alloy at Different Length Scales. Metals (Basel) 11:104. https://doi.org/10.3390/met11010104

3. Verleysen P, Peirs J (2017) Quasi-static and high strain rate fracture behaviour of Ti6Al4V. Int J Impact Eng 108:370–388. https://doi.org/10.1016/j.ijimpeng.2017.03.001

4. Gilles G, Hammami W, Libertiaux V, et al (2011) Experimental characterization and elasto-plastic modeling of the quasi-static mechanical response of TA-6V at room temperature. Int J Solids Struct 48:1277–1289. https://doi.org/10.1016/j.ijsolstr.2011.01.011

5. Tuninetti V, Habraken AM (2014) Impact of anisotropy and viscosity to model the mechanical behavior of Ti–6Al–4V alloy. Mater Sci Eng A 605:39–50. https://doi.org/10.1016/j.msea.2014.03.009

6. Tuninetti V, Flores P, Valenzuela M, et al (2020) Experimental characterization of the

compressive mechanical behaviour of Ti6Al4V alloy at constant strain rates over the full elastoplastic range. Int J Mater Form 13:709–724. https://doi.org/10.1007/s12289-020-01543-2

7. Suryawanshi J, Singh G, Msolli S, et al (2021) Tension-compression asymmetry and shear strength of titanium alloys. Acta Mater 117392. https://doi.org/10.1016/j.actamat.2021.117392

8. Depriester D, Massoni E (2014) On the damage criteria and their critical values for flowforming of ELI grade Ti64. Key Eng Mater 622–623:1221–1227. https://doi.org/10.4028/www.scientific.net/KEM.622-623.1221

9. Bettaieb M Ben, Van Hoof T, Minnebo H, et al (2015) Micromechanics-Based Damage Analysis of Fracture in Ti5553 Alloy with Application to Bolted Sectors. J Mater Eng Perform 24:1262–1278. https://doi.org/10.1007/s11665-015-1383-7

10. Tang B, Wang Q, Guo N, et al (2020) Modeling anisotropic ductile fracture behavior of Ti-6Al-4V titanium alloy for sheet forming applications at room temperature. Int J Solids Struct 207:178–195. https://doi.org/10.1016/j.ijsolstr.2020.10.011

11. Rice JR, Tracey DM (1969) On the ductile enlargement of voids in triaxial stress fields∗. J Mech Phys Solids 17:201–217. https://doi.org/10.1016/0022-5096(69)90033-7

12. Oyane M, Sato T, Okimoto K, Shima S (1980) Criteria for ductile fracture and their applications. J Mech Work Technol 4:65–81. https://doi.org/https://doi.org/10.1016/0378-3804(80)90006-6

13. Quach H, Kim JJ, Nguyen DT, Kim YS (2020) Uncoupled ductile fracture criterion considering secondary void band behaviors for failure prediction in sheet metal forming. Int J Mech Sci 169:105297. https://doi.org/10.1016/j.ijmecsci.2019.105297

14. Ko YK, Lee JS, Huh H, et al (2007) Prediction of fracture in hub-hole expanding process using a new ductile fracture criterion. J Mater Process Technol 187–188:358–362. https://doi.org/10.1016/j.jmatprotec.2006.11.071

15. Cockroft MG, Latham DJ (1968) Ductility and the Workability of Metals. J Inst Met 96:33–39

16. Bao Y, Wierzbicki T (2004) On fracture locus in the equivalent strain and stress triaxiality space. Int J Mech Sci 46:81–98. https://doi.org/10.1016/j.ijmecsci.2004.02.006

17. Bai Y, Wierzbicki T (2008) A new model of metal plasticity and fracture with pressure and Lode dependence. Int J Plast 24:1071–1096. https://doi.org/10.1016/j.ijplas.2007.09.004

18. Tuninetti V, Gilles G, Flores P, et al (2019) Impact of distortional hardening and the strength differential effect on the prediction of large deformation behavior of the Ti6Al4V alloy. Meccanica 54:1823–1840. https://doi.org/10.1007/s11012-019-01051-x

19. Puttick KE (1959) Ductile fracture in metals. Philos Mag 4:964–969. https://doi.org/10.1080/14786435908238272

20. McClintock FA (1968) A Criterion for Ductile Fracture by the Growth of Holes. J Appl Mech 35:363–371. https://doi.org/10.1115/1.3601204

21. Needleman A (1972) Void Growth in an Elastic-Plastic Medium. J Appl Mech 39:964–970. https://doi.org/10.1115/1.3422899

22. Argon AS, Im J, Safoglu R (1975) Cavity formation from inclusions in ductile fracture. Metall Trans A 6:825–837. https://doi.org/10.1007/BF02672306

23. Needleman A, Triantafyllidis N (1978) Void Growth and Local Necking in Biaxially Stretched Sheets. J Eng Mater Technol 100:164–169. https://doi.org/10.1115/1.3443466

24. Chu CC, Needleman A (1980) Void Nucleation Effects in Biaxially Stretched Sheets. J Eng Mater Technol 102:249–256. https://doi.org/10.1115/1.3224807

25. Tvergaard V (1981) Influence of voids on shear band instabilities under plane strain conditions. Int J Fract 17:389–407. https://doi.org/10.1007/BF00036191

26. Goods SH, Brown LM (1983) The Nucleation of Cavities by Plastic Deformation. In: Perspectives in Creep Fracture. Elsevier, pp 71–85

27. Gurson AL (1977) Continuum Theory of Ductile Rupture by Void Nucleation and Growth: Part I—Yield Criteria and Flow Rules for Porous Ductile Media. J Eng Mater Technol 99:2–15. https://doi.org/10.1115/1.3443401

28. Tvergaard V, Needleman A (1984) Analysis of the cup-cone fracture in a round tensile bar. Acta Metall 32:157–169. https://doi.org/10.1016/0001-6160(84)90213-X

29. Leclerc J, Nguyen V-D, Pardoen T, Noels L (2020) A micromechanics-based non-local damage to crack transition framework for porous elastoplastic solids. Int J Plast 127:102631. https://doi.org/10.1016/j.ijplas.2019.11.010

30. Yildiz RA, Yilmaz S (2020) Experimental Investigation of GTN model parameters of 6061 Al alloy. Eur J Mech - A/Solids 83:104040. https://doi.org/10.1016/j.euromechsol.2020.104040

31. Wu H, Zhuang X, Zhao Z (2022) Extended GTN model for predicting ductile fracture under a broad range of stress states. Int J Solids Struct 239–240:111452. https://doi.org/10.1016/j.ijsolstr.2022.111452

32. Shahzamanian MM, Wu PD (2021) Study of forming limit diagram (FLD) prediction of anisotropic sheet metals using Gurson model in M-K method. Int J Mater Form 14:1031–1041. https://doi.org/10.1007/s12289-021-01619-7

33. Rojas-Ulloa C, Valenzuela M, Tuninetti V, Habraken A-M (2021) Identification and validation of an extended Stewart-Cazacu micromechanics damage model applied to Ti–6Al–4V specimens exhibiting positive stress triaxialities. Proc Inst Mech Eng Part L J Mater Des Appl 235:1248–1261. https://doi.org/10.1177/14644207211009933

34. Stewart JB, Cazacu O (2011) Analytical yield criterion for an anisotropic material containing spherical voids and exhibiting tension–compression asymmetry. Int J Solids Struct 48:357–373. https://doi.org/10.1016/j.ijsolstr.2010.10.009

35. Kim M, Lee H, Park N (2022) Evaluation of deformation for titanium alloy sheet in single point incremental forming based on asymmetric yield function. Int J Mater Form 15:1–12. https://doi.org/10.1007/s12289-022-01712-5

36. Sandoval CFB, Malcher L, Canut FA, et al (2020) Micromechanical Gurson-based continuum damage under the context of fretting fatigue: Influence of the plastic strain field. Int J Plast 125:235–264. https://doi.org/10.1016/j.ijplas.2019.09.012

37. Cazacu O, Plunkett B, Barlat F (2006) Orthotropic yield criterion for hexagonal closed packed metals. Int J Plast 22:1171–1194. https://doi.org/10.1016/j.ijplas.2005.06.001

38. MSM & GEG (ULiege) (2022) Lagamine software. In: Univ. Liege

39. Tuninetti V, Gilles G, Péron-Lührs V, Habraken AM (2012) Compression test for metal characterization using digital image correlation and inverse modeling. Procedia IUTAM 4:206–214. https://doi.org/10.1016/j.piutam.2012.05.022

40. Rojas-Ulloa C, Bouffioux C, Jaramillo AF, et al (2021) Nanomechanical Characterization of the Deformation Response of Orthotropic Ti–6Al–4V. Adv Eng Mater 23:2001341. https://doi.org/10.1002/adem.202001341

41. Cescotto S, Charlier R (1993) Frictional contact finite elements based on mixed variational principles. Int J Numer Methods Eng 36:1681–1701. https://doi.org/10.1002/nme.1620361005

42. Habraken AM, Cescotto S (1998) Contact between deformable solids: The fully coupled approach. Math Comput Model 28:153–169. https://doi.org/10.1016/S0895-7177(98)00115-0

43. Morch H, Duchêne L, Harzallah R, et al (2021) Efficient temperature dependence of parameters for thermo-mechanical finite element modeling of alloy 230. Eur J Mech - A/Solids 85:104116. https://doi.org/10.1016/j.euromechsol.2020.104116

44. Yuan S, Duchêne L, Keller C, et al (2020) Tunable surface boundary conditions in strain gradient crystal plasticity model. Mech Mater 145:103393. https://doi.org/10.1016/j.mechmat.2020.103393

45. Chen G, Caudill J, Ren C, Jawahir IS (2022) Numerical modeling of Ti-6Al-4V alloy orthogonal cutting considering microstructure dependent work hardening and energy density-based failure behaviors. J Manuf Process 82:750–764. https://doi.org/10.1016/j.jmapro.2022.08.032

46. Katani S, Madadi F, Atapour M, Ziaei Rad S (2013) Micromechanical modelling of damage behaviour of Ti-6Al-4V. Mater Des 49:1016–1021. https://doi.org/10.1016/j.matdes.2013.02.021

47. Lecarme L, Maire E, Kumar K.C. A, et al (2014) Heterogenous void growth revealed by in situ 3-D X-ray microtomography using automatic cavity tracking. Acta Mater 63:130–139. https://doi.org/10.1016/j.actamat.2013.10.014

48. Cazacu O, Revil-Baudard B, Chandola N (2019) Plasticity-Damage Couplings: From Single Crystal to Polycrystalline Materials. Springer International Publishing, Cham

49. Rym Harbaoui, Olfa Daghfas, Amna Znaidi, Victor Tuninetti (2020) Mechanical behavior of materials with a compact hexagonal structure obtained by an advanced identification strategy of HCP material, AZ31B-H24. Frat ed Integrità Strutt 14:295–305. https://doi.org/10.3221/IGF-ESIS.53.23

50. Zhang Z., Thaulow C, Ødegård J (2000) A complete Gurson model approach for ductile fracture. Eng Fract Mech 67:155–168. https://doi.org/10.1016/S0013-7944(00)00055-2

51. Tvergaard V (1982) On localization in ductile materials containing spherical voids. Int J Fract 18:237–252. https://doi.org/doi.org/10.1007/BF00015686

52. Perrin G, Leblond JB (1990) Analytical study of a hollow sphere made of plastic porous material and subjected to hydrostatic tension-application to some problems in ductile fracture of metals. Int J Plast 6:677–699. https://doi.org/10.1016/0749-6419(90)90039-H

53. Seidenfuss M, Linse T (2016) Recent Trends in Fracture and Damage Mechanics. Springer International Publishing, Cham

54. Thomason PF (1993) Ductile fracture by the growth and coalescence of microvoids of non-uniform size and spacing. Acta Metall Mater 41:2127–2134. https://doi.org/10.1016/0956-7151(93)90382-3

55. Tvergaard V (1998) Interaction of very small voids with larger voids. Int J Solids Struct 35:3989–4000. https://doi.org/10.1016/S0020-7683(97)00254-0

56. Tvergaard V, Hutchinson JW (2002) Two mechanisms of ductile fracture: void by void growth versus multiple void interaction. Int J Solids Struct 39:3581–3597. https://doi.org/10.1016/S0020-7683(02)00168-3

57. Liu B, Qiu X, Huang Y, et al (2003) The size effect on void growth in ductile materials. J Mech Phys Solids 51:1171–1187. https://doi.org/10.1016/S0022-5096(03)00037-1

58. Benzerga A., Besson J, Pineau A (2004) Anisotropic ductile fracture Part I: experiments. Acta Mater 52:4623–4638. https://doi.org/10.1016/j.actamat.2004.06.020

59. Xue L (2008) Constitutive modeling of void shearing effect in ductile fracture of porous materials. Eng Fract Mech 75:3343–3366. https://doi.org/10.1016/j.engfracmech.2007.07.022

60. Luo T, Gao X (2018) On the prediction of ductile fracture by void coalescence and strain localization. J Mech Phys Solids 113:82–104. https://doi.org/10.1016/j.jmps.2018.02.002

61. Benzerga AA, Besson J, Pineau A (2004) Anisotropic ductile fracture Part II: theory. Acta Mater 52:4639–4650. https://doi.org/10.1016/j.actamat.2004.06.019

62. Butcher C, Chen Z, Bardelcik A, Worswick M (2009) Damage-based finite-element modeling of tube hydroforming. Int J Fract 155:55–65. https://doi.org/10.1007/s10704-009-9323-x

63. Pardoen T, Doghri I, Delannay F (1998) Experimental and numerical comparison of void growth models and void coalescence criteria for the prediction of ductile fracture in copper bars. Acta Mater 46:541–552. https://doi.org/10.1016/S1359-6454(97)00247-4

64. Pardoen T, Hutchinson J. (2000) An extended model for void growth and coalescence. J Mech Phys Solids 48:2467–2512. https://doi.org/10.1016/S0022-5096(00)00019-3

65. Pardoen T, Hutchinson JW (2003) Micromechanics-based model for trends in toughness

of ductile metals. Acta Mater 51:133–148. https://doi.org/10.1016/S1359-6454(02)00386-5

66. Ragab AR (2004) A model for ductile fracture based on internal necking of spheroidal voids. Acta Mater 52:3997–4009. https://doi.org/10.1016/j.actamat.2004.05.015

67. Ragab AR (2004) Application of an extended void growth model with strain hardening and void shape evolution to ductile fracture under axisymmetric tension. Eng Fract Mech 71:1515–1534. https://doi.org/10.1016/S0013-7944(03)00216-9

68. Lassance D, Scheyvaerts F, Pardoen T (2006) Growth and coalescence of penny-shaped voids in metallic alloys. Eng Fract Mech 73:1009–1034. https://doi.org/10.1016/j.engfracmech.2005.12.004

69. Betaieb E, Yuan S, Guzman CF, et al (2019) Prediction of cracks within cones processed by single point incremental forming. Procedia Manuf 29:96–104. https://doi.org/10.1016/j.promfg.2019.02.111

70. de Montleau P, Habraken AM, Duchêne L (2008) A new finite element integration scheme. Application to a simple shear test of anisotropic material. Int J Numer Methods Eng 73:1395–1412. https://doi.org/10.1002/nme.2130

71. Badreddine H, Yue ZM, Saanouni K (2017) Modeling of the induced plastic anisotropy fully coupled with ductile damage under finite strains. Int J Solids Struct 108:49–62. https://doi.org/10.1016/j.ijsolstr.2016.10.028

72. Jiang W, Li Y, Su J (2016) Modified GTN model for a broad range of stress states and application to ductile fracture. Eur J Mech - A/Solids 57:132–148. https://doi.org/10.1016/j.euromechsol.2015.12.009

73. Jedidi MY, Bouguecha A, Khabou MT, Haddar M (2021) An Anisotropic Model with Non-associated Flow Rule to Predict HCP Sheet Metal Ductility Limit. Springer International Publishing

74. Simo JC, Hughes TJR (1999) Computational inelasticity. Comput Math with Appl 37:134. https://doi.org/10.1016/S0898-1221(99)90277-8

75. Tuninetti V, Gilles G, Milis O, et al (2015) Anisotropy and tension–compression asymmetry modeling of the room temperature plastic response of Ti–6Al–4V. Int J Plast 67:53–68. https://doi.org/10.1016/j.ijplas.2014.10.003

76. Geuzaine C, Remacle J-F (2009) Gmsh: A 3-D finite element mesh generator with built-in pre- and post-processing facilities. Int J Numer Methods Eng 79:1309–1331. https://doi.org/10.1002/nme.2579

77. Duchêne L, El Houdaigui F, Habraken AM (2007) Length changes and texture prediction during free end torsion test of copper bars with FEM and remeshing techniques. Int J Plast. https://doi.org/10.1016/j.ijplas.2007.01.008

78. Enakoutsa K (2014) An improved nonlocal Gurson model for plastic porous solids, with an application to the simulation of ductile rupture tests. Appl Math Model 38:2791–2799. https://doi.org/10.1016/j.apm.2013.11.007

79. Nguyen V-D, Pardoen T, Noels L (2020) A nonlocal approach of ductile failure incorporating void growth, internal necking, and shear dominated coalescence mechanisms. J Mech Phys Solids 137:103891. https://doi.org/10.1016/j.jmps.2020.103891

80. Duchêne L, Habraken AM (2005) Analysis of the sensitivity of FEM predictions to numerical parameters in deep drawing simulations. Eur J Mech - A/Solids 24:614–629. https://doi.org/10.1016/j.euromechsol.2005.04.007

81. Betaieb E, Duchêne L, Habraken AM (2022) Calibration of kinematic hardening parameters on sheet metal with a Computer Numerical Control machine. Int J Mater Form 15:. https://doi.org/10.1007/s12289-022-01714-3

82. Koplik J, Needleman A (1988) Void Growth and Coalescence in Porous. Int J Solids Struct 24:835–853

83. Tuninetti V, Yuan S, Gilles G, et al (2016) Modeling the ductile fracture and the plastic anisotropy of DC01 steel at room temperature and low strain rates. J Phys Conf Ser 734:032075. https://doi.org/10.1088/1742-6596/734/3/032075